Molecular Cancer

RESEARCH

Open Access

o8G-modified circPLCE1 inhibits lung cancer progression via chaperone-mediated autophagy

Qingyun Zhao[1,2†], Dunyu Cai[1,2†], Haotian Xu[1,2†], Yihong Gao[1,2], Ruirui Zhang[1,2], Xiaodong Zhou[1,2], Xingcai Chen[1,2], Sixian Chen[1,2], Jiaxi Wu[1,2], Wenyi Peng[1,2], Shengyi Yuan[1,2], Deqing Li[1,2], Gang Li[1,2*] and Aruo Nan[1,2*]

Abstract

Background Lung cancer poses a serious threat to human health, but its molecular mechanisms remain unclear. Circular RNAs (circRNAs) are closely associated with tumour progression, and the important role of 8-oxoguanine (o8G) modification in regulating the fate of RNA has been gradually revealed. However, o8G modification of circRNAs has not been reported. We identified circPLCE1, which is significantly downregulated in lung cancer, and further investigated the o8G modification of circPLCE1 and the related mechanism in lung cancer progression.

Methods We identified differentially expressed circRNAs by RNA high-throughput sequencing and then conducted methylated RNA immunoprecipitation (MeRIP), immunofluorescence (IF) analysis, crosslinking immunoprecipitation (CLIP) and actinomycin D (ActD) assays to explore circPLCE1 o8G modification. The biological functions of circPLCE1 in vivo and in vitro were clarified via establishing a circPLCE1 silencing/overexpression system. Tagged RNA affinity purification (TRAP), RNA Immunoprecipitation (RIP) and coimmunoprecipitation (Co-IP) assays, and pSIN-PAmCherry-KFERQ-NE reporter gene were used to elucidate the molecular mechanism by which circPLCE1 inhibits lung cancer progression.

Results This study revealed that reactive oxygen species (ROS) can induce circPLCE1 o8G modification and that AUF1 can mediate a decrease in circPLCE1 stability. We found that circPLCE1 significantly inhibited lung cancer progression in vitro and in vivo and that its expression was associated with tumour stage and prognosis. The molecular mechanism was elucidated: circPLCE1 targets the HSC70 protein, increases its ubiquitination level, regulates ATG5-dependent macroautophagy via the chaperone-mediated autophagy (CMA) pathway, and ultimately inhibits lung cancer progression.

†Qingyun Zhao, Dunyu Cai and Haotian Xu contributed equally to this work.

*Correspondence:
Gang Li
ligang@gxmu.edu.cn
Aruo Nan
nanaruo@163.com
Full list of author information is available at the end of the article

Conclusion o8G-modified circPLCE1 inhibits lung cancer progression through CMA to inhibit macroautophagy and alter cell fate. This study provides not only a new theoretical basis for elucidating the molecular mechanism of lung cancer progression but also potential targets for lung cancer treatment.

Keywords CircRNA, O8G modification, HSC70, Molecular chaperone-mediated autophagy, Lung cancer

Graphical abstract

ROS induce circPLCE1 o8G modification, and AUF1 specifically recognizes o8G modification, thereby decreases circPLCE1 stability. circPLCE1 targets the HSC70 protein, increases its ubiquitination level, inhibits CMA activity, and promotes ATG5-dependent macroautophagy via the CMA pathway, altering the fate of tumour cells and ultimately inhibiting lung cancer progression.

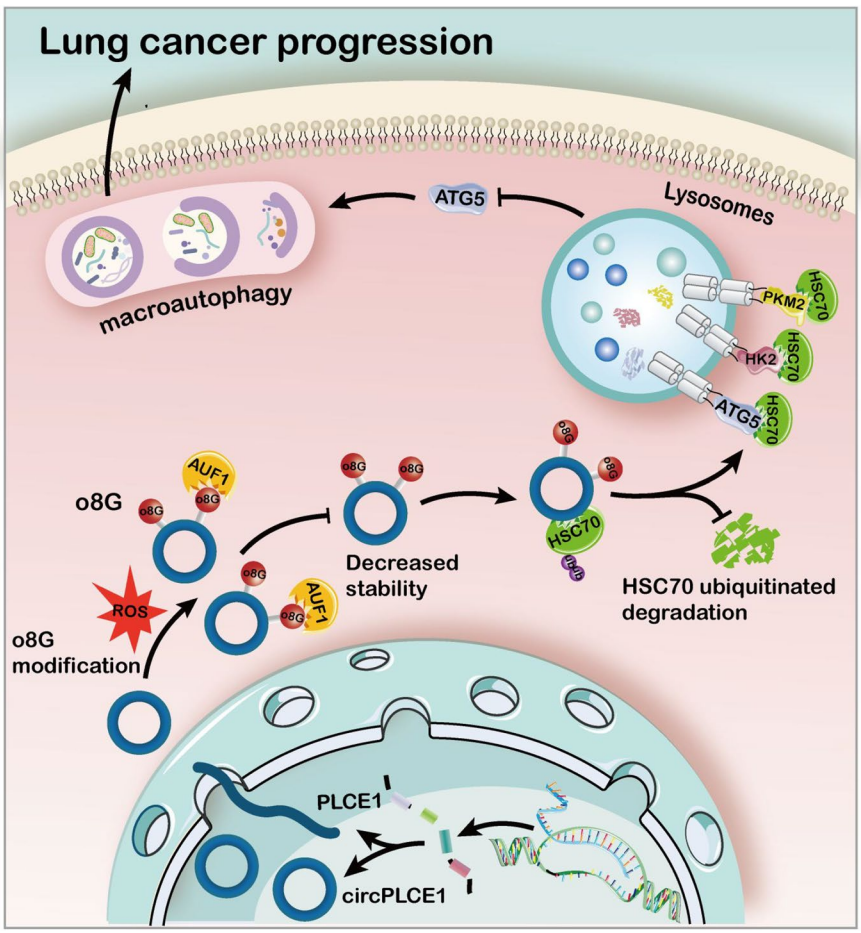

Introduction

Lung cancer is a serious public health problem worldwide and the leading cause of cancer-related death. Recent studies have revealed that, globally, lung cancer ranks first in terms of morbidity and mortality [1, 2]. Recently, the development of drugs targeting specific gene products has greatly improved the treatment of patients with lung cancer, but the prognosis of lung cancer remains poor [3, 4]. Therefore, it is important to study the mechanisms of lung cancer progression in depth and explore new therapeutic targets for lung cancer. Although many coding genes and non-coding RNAs are involved in the process of lung cancer progression [5–8], the specific molecular mechanisms involved remain unclear.

Circular RNAs (circRNAs) are a class of RNAs produced by back-splicing that have a covalently closed loop

structure without a 5' cap or a 3' poly(A) tail [9, 10]. With the iterative updating of sequencing techniques and bioinformatic algorithms, many circRNAs have been found to be differentially expressed in a wide range of malignant tumours, and the biological functions of circRNAs in tumours have been revealed [8, 11, 12]. Studies have revealed that circRNAs play important roles in tumour progression through a variety of functional mechanism; for example, they can act as microRNA (miRNA) sponges [13] or bind directly to mRNAs [14] or proteins [15, 16]. As research has intensified, circRNAs are also thought to be translated into peptides [17]. Owing to their unique expression pattern, high stability and tissue specificity, circRNAs have attracted much attention in cancer diagnosis and therapy. However, the molecular mechanisms of circRNAs in lung cancer have not been fully elucidated. In our previous study on lung carcinogenesis [18], we found that circPLCE1 expression was dysregulated in a sodium arsenite-induced malignant cell transformation model, suggesting that circPLCE1 may have an important function in lung carcinogenesis. To explore whether circPLCE1 may play a biological function in lung cancer progression, we examined the expression of circPLCE1 in lung cancer cell lines. The results showed that circPLCE1 was significantly downregulated in lung cancer cell lines compared to BEAS-2B cells. Subsequently, examination of circPLCE1 expression in lung cancer tissues and paracancerous tissues revealed that circPLCE1 was significantly downregulated in lung cancer tissues, which indicate that circPLCE1 may play a key role in the progression of lung cancer. Therefore, circPLCE1 was selected for in-depth exploration in this study.

Although the number of studies on the role of circRNAs in tumorigenesis and tumour progression is increasing, most related studies still focus mainly on the regulation of downstream genes and signalling pathways by circRNAs, and little is known about the upstream molecular mechanisms of circRNAs. The emergence of RNA modifications has resulted in new ideas for elucidating the mechanism of altered expression of circRNA itself and its functional research in malignant tumours [19–22]. Research suggests that three classes of molecules are involved in the process of RNA modification: RNA-modifying enzymes (writers), which transfer specific chemical groups to the RNA molecule; eraser proteins (erasers), which remove specific chemical groups from modified nucleotides, restoring their unmodified state; and RNA-binding proteins (readers), which specifically recognize modified nucleotides [19–21]. With in-depth research related to RNA modifications, the important roles of the o8G modification in regulating both the fate of RNA molecules and their important roles in pathology and physiology have been revealed. The results of the present study suggest that the o8G modification does not involve a writer but rather that it is an oxidative modification that occurs when reactive oxygen species (ROS) attack guanine bases in RNA molecules [23]. o8G modification can change the base pairing mode of RNA, transforming the original G–C pairing of RNAs into G–A pairing. In the rat H9c2 myocardial cell line, oxidized miR-184 facilitates the initiation of apoptosis by re-targeting Bcl-xl and Bcl-w [24]. The o8G modification of the miR-1 seed region also affects the specificity of targeting downstream genes to induce cardiac hypertrophy [25]. 4o8G-miR-124 and 4o8G-let-7 inhibit the progression of gliomas, and 3o8G-miR-122 and 4o8G-let-7 modulate tumour-promoting signalling pathways to promote hepatocellular carcinoma progression [26]. It has even been shown that o8G modification can mediate the rapid degradation of an RNA and affect its stability through multiple pathways [27]. o8G-modified RNAs are also recognized by specific RNA-binding proteins (readers) and are degraded via unknown mechanisms [28–30]. With the discovery of miRNA o8G modifications, the important epigenetic role of o8G modifications has been gradually revealed, but the o8G modification of circRNAs has not been reported.

With the deepening of circRNA-related research, circRNAs are thought to play important roles in the biological process of autophagy [31]. Autophagy is a cellular process that mediates the lysosome-dependent degradation of organelles, proteins, etc., and is closely associated with a variety of diseases, including tumours, and plays a bidirectional role in cell survival and death [32–35]. Autophagy can be categorized into three types according to the manner in which the cargos to be degraded are captured: macroautophagy, microautophagy, and chaperone-mediated autophagy (CMA) [36]. Although the mechanism by which circRNAs affect tumorigenesis and tumour progression through macroautophagy has been revealed [37, 38], circRNAs that target CMA have not been elucidated. CMA is a type of selective autophagy characterized mainly by its lack of involvement of membrane transport vesicles and selectivity for cargo [39]. CMA mainly degrades cytoplasmic proteins with KEFRQ-like motifs; these proteins are recognized by the chaperone protein HSC70 and are transported to lysosomes via the LAMP-2A transporter for protein quality control [39]. Recent studies revealed that CMA is consistently upregulated in primary tumours, such as lung, hepatocellular carcinoma, melanoma, and gastric, colon, ovarian, and breast tumours [40], and is downregulated in only a few malignancies, such as acute myeloid leukaemia [41]. Accumulating genetic evidence indicates the therapeutic value of targeting CMA in cancer; however, effective means of inhibiting CMA are lacking. The

expansion of circRNA-related research has provided new insights into targeting CMA and thus the development of antitumour therapeutics.

In this study, we found that circPLCE1 is significantly downregulated in lung cancer cell lines and lung cancer tissues, and that circPLCE1 expression was significantly associated with the stage, tumour size, and prognosis of lung cancer. We reported the ground-breaking finding that o8G modification occurs on circRNA; intracellular ROS induce o8G modification, and AUF1 specifically recognizes o8G modification, thereby decreasing circPLCE1 stability and expression. We clarified that circPLCE1 has a biological function in inhibiting lung cancer progression both in vitro and in vivo. Moreover, we discovered that ATG5 can act as a novel CMA substrate. We elucidated the novel molecular mechanism by which o8G-modified circPLCE1 targets HSC70, increases its ubiquitination level, decreases CMA activity, and regulates ATG5-dependent macroautophagy through the CMA pathway, thus altering the fate of tumour cells and ultimately inhibiting lung cancer progression. Overall, this study revealed that o8G modification occurs on a circRNA and indicates that the o8G-modified circRNA can play an important role in lung cancer progression. This study provides new insights regarding the molecular mechanisms of lung cancer progression and may facilitate the development of lung cancer treatment methods.

Methods

Cell culture

The normal human bronchial epithelial cells (BEAS-2B) and lung cancer cells (A549, H1299, H226, H460, and H2170) used in this study were obtained from the American Type Culture Collection (ATCC). 293T cells used in this study were obtained from Guangzhou Cellcook Biotech Co., Ltd (Guangzhou, China). BEAS-2B cells were cultured in BEGM (Lonza, CC-3171) medium; H1299, H226, H460 and H2170 cells were cultured in RPMI-1640 medium containing 10% foetal bovine serum (FBS; Gibco, 10099141C) and 1% penicillin–streptomycin (Gibco, 1514022); A549 cells were cultured in Ham's F-12K medium containing 10% FBS (Gibco, 10099141C) and 1% penicillin–streptomycin; and 293 T cells were cultured in DMEM containing 10% FBS (Gibco, 10099141C) and 1% penicillin–streptomycin (Gibco, 1514022). All the cells were cultured at 37 °C in a 5% CO_2 incubator and tested negative for mycoplasma contamination.

High-throughput RNA sequencing

In previous studies, we used BEAS-2B human bronchial mucosal epithelial cells exposed to arsenic to establish a cell model of arsenic-induced malignant transformation (BEAS-2B-As). (For details, please refer to the study on the mechanism of action of circBRWD1 in arsenic-induced lung cancer.) The extracted total RNA was fragmented into short sections in fragmentation buffer and then converted into 1st-strand cDNA via reverse transcription with random hexamer primers. The second strand was synthesized via deoxyribonucleoside triphosphate (dNTP), RNase H and DNA polymerase I. The cDNA fragment was purified via QiaQuick PCR, the ends were repaired, and base A was introduced. Sequencing was performed on an Illumina HiSeqTM 2500 at Gene Denovo Biotechnology (Guangzhou, China) after PCR amplification. Differential circRNA expression profiles were successfully generated (Supplementary Table 1).

The differentially expressed circRNAs were screened according to "$P < 0.1$" and "$\log_2$-fold change ($\log_2$ FC) > 2" and visualised in volcano plots. The differentially expressed circRNAs with "$\log_2$ FC > 2" were screened for clustering analysis. The clustering method was "complete", and the distance method was "Euclidean".

RNA extraction and RT–qPCR

Total RNA was extracted from the tissue and cellular samples with TRIzol reagent (Invitrogen, 15596018), and the RNA concentrations were measured via a Nanodrop One spectrophotometer (Thermo Fisher Scientific, ND-ONEC-W). Reverse transcription was subsequently performed using the GoScript™ Reverse Transcription System (Promega, A5001). For the qPCR analysis of circRNAs, we used the principle of crossing cleavage sites to design a divergent primer specific for circRNAs. The qPCR primers (Sangon Biotech, Shanghai, China) were diluted to 10 μmol (see Supplementary Table 2 for primer sequences). qPCR was performed via a GoTaq® qPCR Master Mix (Promega, A6001) kit. The target RNA levels were normalized to the GAPDH mRNA level in each sample.

Lung cancer tissue samples

The lung cancer and paraneoplastic clinical tissue samples used in this study were obtained from the First Affiliated Hospital of Guangxi Medical University. Each patient signed an informed consent form before surgery. Human materials were obtained with patient consent and approved by the Ethics Committee of the First Affiliated Hospital of Guangxi Medical University. The relative expression of circPLCE1 in lung cancer tissues was assessed via qPCR, and the median relative expression was calculated. The samples whose relative expression value for circPLCE1 was greater than the median were categorized into the high-expression group, and those whose relative expression of circPLCE1 was less than the

median expression were categorized into the low-expression group.

Prediction of biological function

We used catRAPID (http://service.tartaglialab.com/page/catrapid_group) for the prediction of direct binding proteins of circPLCE1 and the DAVID database (https://david.ncifcrf.gov/) for the KEGG analysis (see Supplementary Fig. 1a.). For Supplementary Fig. 1b, the circBANK (http://www.circbank.cn/), TargetScanHuman 8.0 (https://www.targetscan.org/vert_80/) and miRBD (https://mirdb.org/) databases were used to predict circPLCE1-targeted miRNAs; five miRNAs, namely, hsa-miR-6885-3P, hsa-miR-3174, hsa-miR-4482-5P, hsa-miR-8485, and hsa-miR-593-3P, were obtained by taking the intersections of the miRNAs predicted by the three databases. Published studies on PubMed (https://pubmed.ncbi.nlm.nih.gov/) indicate that hsa-miR-593-3P and hsa-miR-8485 might be potential oncogenes, which is inconsistent with the expression trend of circPLCE1 in lung cancer; thus, these genes were excluded. Subsequently, TargetScanHuman 8.0, miRBD, and miPID (http://ophid.utoronto.ca/mirDIP/index.jsp) were used to predict hsa-miR-6885-3P, hsa-miR-3174 and hsa-miR-4482-5P targeted mRNAs, and the mRNAs targeted by the three miRNAs were intersected for further analysis. Finally, KEGG analysis was performed via DAVID.

Transfection

siRNAs targeting circPLCE1, ATG5, and AUF1 were designed (RiboBio, Guangzhou, China). The siRNA target sequence information is shown in Supplementary Table 2. The cells were seeded at a density of 2.5×10^6 cells/well in 6-well plates or 6×10^4 cells/well in 96-well plates and cultured for 12–18 h before siRNA transfection was performed via the riboFECT CP Kit (RiboBio, C10511-05). The siRNA concentration used for transfection was 100 nM, and culture was continued for 48 h after transfection before subsequent experiments were carried out. The circPLCE1 transient overexpression plasmid was constructed via the pcircRNA 2.2 hsa vector (Supplementary Fig. 1c), and the HSC70 transient overexpression plasmid was constructed using the pCMV-SPORT6 vector (Fenghui Biotechnology, Changsha, China); the plasmids were purified using a plasmid mini kit (Biomiga, BW-PD1211-03). The cells were seeded at a density of 3.5×10^6 cells/well in 6-well plates or 1×10^5 cells/well in 96-well plates, and after further incubation for 12–18 h, the overexpression plasmids were transfected via the Lipofectamine™ 3000 Transfection Kit (Invitrogen, L3000015). The cells in the 6-well plates were transfected with 2.5 μl (1000 ng/μl) per well, and the cells in the 96-well plates were transfected with 0.5 μl (1000 ng/μl) per well. The medium containing 10% FBS was replaced with new medium 8 h post-transfection, and subsequent experiments were carried out after 48 h of continued incubation.

Lentiviral infection and stable transfection cell line construction

The circPLCE1 stable overexpression plasmid was constructed via the V53B plv-puro-circRNA-Hsa vector (IEMed, Guangzhou, China) (Supplementary Fig. 1d). A total of 4×10^6 293 T cells were inoculated into 6-well plates, after which 2 μg of the circPLCE1 stable overexpression plasmid, 1.2 μg of PMD2.G, and 1.2 μg of PSPAX were added for cotransfection into 293 T cells using PolyJet™ In Vitro Transfection Reagent (Cisco Biotech Co., Ltd., Jinan, China). The mixture was incubated in a 5% CO_2 incubator for 72 h. Viral supernatants were collected by centrifugation at 3000 rpm for 30 min. The viral supernatant was collected and centrifuged at 3000 rpm for 30 min. A549 cells were inoculated into 6-well plates at 2×10^6 million/well and transduced with viral supernatant after cell attachment. The cells were incubated at 37 °C in a 5% CO_2 incubator, and the fluorescence intensity was observed under a fluorescence microscope after 48 h. A stable circPLCE1-overexpressing cell line was constructed via the puromycin screening method.

Flow cytometry to detect ROS levels

A ROS assay kit (Beyotime, S0033S) was used to detect the cellular ROS levels. DCFH-DA was diluted with serum-free culture solution at a ratio of 1:1000 to a final concentration of 10 μM/L. One millilitre of DCFH-DA was added, and the mixture was incubated at 37 °C in a 5% CO_2 incubator for 20 min. Then, 1×PBS was used to wash the cells three times. The cells were digested with trypsin, collected via centrifugation, washed with 1×PBS and resuspended by adding 500 μL of 1×PBS, and the ROS level was detected via flow cytometry (Beckman Coulter, Miami, USA).

Cell viability assay

Cell viability was determined using Cell Counting Kit-8 (CCK-8; Dojindo, CK04) assays. A549 and H1299 cells were seeded in 96-well plates, transfected with siRNAs/overexpression plasmids and cultured for 48 h. The working solution was prepared at a 1:10 ratio of CCK-8 reagent:medium containing 10% FBS. The working solution was added to the wells (100 μl/well), and the plates were incubated at 37 °C for 1.5 h. The absorbance of the cells at 450 nm was measured.

EdU incorporation assay

The Cell Light EdU Apollo 567 In Vitro Kit (RiboBio, C10310-1) was used to evaluate cell proliferation. A549 cells and H1299 cells were seeded in 96-well plates, transfected with siRNAs/overexpression plasmids, and cultured for 48 h. The cells were fixed with 4% paraformaldehyde (PFA%), and staining solutions were prepared for Apollo staining and DNA staining according to the manufacturer's instructions. The cells were imaged via the EVOS® FL Auto Imaging System, and ImageJ was used for statistical analysis of the DAPI-positive and EdU-positive cells.

Detection of apoptosis by flow cytometry

An Annexin V-FITC/Propidium Iodide (PI) Double Staining Apoptosis Detection Kit (KeyGen Biotech, KGA107) was used to determine the proportion of apoptotic cells. A549 cells and H1299 cells were seeded in 6-well plates, and the culture was continued for 48 h after siRNA/overexpression plasmid transfection. The cell culture medium was collected, and the cells were detached from the plates with EDTA-free trypsin (Solarbio, T1350) and centrifuged at 2000 rpm for collection. The cells were then resuspended in binding buffer, and 5 μl of Annexin V-FITC and 5 μl of PI were added sequentially. Detection of apoptosis was performed using a CytoFLEX flow cytometer (Beckman Coulter, Miami, USA).

Cell cycle analysis by flow cytometry

The Cell Cycle Assay Kit (KeyGen Biotech, KGA511) was used to analyse the cell cycle. A549 cells and H1299 cells were seeded in 6-well plates, and culture was continued for 48 h after siRNA/overexpression plasmid transfection. The cells were detached and collected, fixed in a solution of 7:3 anhydrous ethanol: PBS, and incubated at −20 °C overnight. After centrifugation, the ethanol was removed by washing with PBS, and 30 μl of RNase was added for incubation at 37 °C for 30 min. Then, 120 μl of PI solution was added for incubation at 4 °C for 30 min in the dark. Cell cycle analysis was performed with a CytoFLEX flow cytometer (Beckman Coulter, Miami, USA).

Transwell migration assay

A549 cells and H1299 cells were seeded in 6-well plates, and the culture was continued for 48 h after siRNA/overexpression plasmid transfection. The migration chambers (Corning, Corning, USA) were equilibrated at 37 °C for 1 h in serum-free culture medium. After the cells were detached and collected, they were resuspended in serum-free medium and counted. Then, 1×10^4 cells were seeded in each migration chamber, and medium containing 10% FBS was added to the lower compartment for incubation at 37 °C for 24 h. After the cells were washed with PBS and fixed with methanol for 20 min, they were stained with crystal violet, and the upper layer of cells in the chambers was removed by wiping. After drying, the cells were imaged using an EVOS® FL Auto Imaging System, and statistical analysis was performed with ImageJ.

Wound healing assay

A549 cells and H1299 cells were seeded in 6-well plates, and the culture was continued for 48 h after siRNA/overexpression plasmid transfection. When the cells were approximately 90% confluent, a scratch of uniform width was made on the cell surface, the cells were washed with PBS, and the medium was changed to medium containing 10% FBS. Images of the same location in the scratch wound were acquired at 0 h and 24 h using a microscope (Olympus, Tokyo, Japan), and the area of the scratch at each time point was calculated for statistical analysis.

Subcutaneous tumorigenesis assay in nude mice

Four-week-old female BALB/c nude mice were purchased from Guangxi Medical University Laboratory Animal Centre. We used a previously published method for generating a subcutaneous xenograft tumour model in nude mice and used seven nude mice per group to conduct the experiments. The nude mice were housed at the SPF-level Experimental Animal Center of Guangxi Medical University. The nude mice were randomly divided into two groups: those injected with A549 cells with stable circPLCE1 overexpression or those injected with control A549 cells into the right dorsal surface. The survival status of the nude mice was monitored at three-day intervals. The diameters of the tumours were measured by using Vernier callipers ($\text{volume}=\text{length}\times\text{height}^2\times0.5$), and the nude mice were weighed. The experimental animals were sacrificed after 21 days of tumour formation, and immunohistochemistry and western blotting were conducted after tumour excision. The animal experiments conducted in this study were approved by the Experimental Animal Ethics Committee of Guangxi Medical University, and all experimental operations were conducted in compliance with international guidelines.

FISH

circPLCE1-specific FISH probes were designed (Sangon Biotech Ltd., Shanghai, China) (see Supplementary Table 2). The subcellular localization of circPLCE1 in A549 cells and H1299 cells was determined via a FISH kit (RiboBio, C10910). The cells were seeded in 12-well plates containing microscope cover glasses at a density of 2×10^5 cells/well, and after the cells had adhered to the plates, they were fixed with 4% PFA. The cells were permeabilized via incubation in permeabilization buffer (0.5% Triton X-100 in PBS) for 5 min, and the hybridization

reaction mixture was prepared at a probe:hybridization solution ratio of 1:19. The cells were incubated at 42 °C for 16 h in the dark after the addition of the hybridization solution. This incubation step was followed by DAPI staining and fluorescence imaging using an LSM800 confocal microscope (Zeiss, Oberkochen, Germany).

Cellular nuclear–cytoplasmic separation

A PARIS™ kit (Invitrogen, AM1921) was used to perform nuclear–cytoplasmic separation to determine the subcellular localization of circPLCE1. A549 and H1299 cells (1×10^7) were collected and lysed on ice after the addition of cell fractionation buffer. The supernatant was separated from the precipitate, 2×lysis/binding solution was added, and the mixture was mixed well. The mixture was added to a filter column and centrifuged at 4 °C and 10,000×*g* for 1 min, after which the filtrate was discarded. Then, 700 μl of wash solution was added to wash the column, the column was centrifuged at 10,000×*g* for 1 min at 4 °C, and the filtrate was discarded. Then, 50 μl of ES solution was added, and the column was allowed to stand at 4 °C for 15 min prior to centrifugation at 4 °C and 10,000×*g* for 1 min to collect RNA. circPLCE1 expression was measured via RT–qPCR with GAPDH as a cytoplasmic marker and U6 as a nuclear marker.

Western blot analysis and antibodies

Cell lysis buffer (10 mM Tris–HCl (pH 7.4), 1% sodium dodecyl sulphate (SDS), and 1 mM Na_3VO_4) was prepared, and the cells were lysed on ice for 5 min. The protein samples were denatured at 100 °C for 5 min and subjected to ultrasonic disruption. Protein quantification was performed using the Pierce™ BCA Protein Assay Kit (Thermo Fisher Scientific, 23227). Proteins were separated on an SDS–polyacrylamide gel and then transferred to a membrane at a constant current of 200 mA for 1.5 h. Blocking buffer was prepared with 5% skim milk, and the primary antibody was added for incubation overnight on a shaker at 4 °C. After the membrane was washed with TBS, the corresponding secondary antibody was added for incubation at room temperature for 1 h. Antibody binding was detected using an enhanced chemiluminescence (ECL) kit, and images were acquired via a chemiluminescence imager and quantitatively analysed via ImageJ software. The primary antibodies used in this study were as follows: anti-HSC70 (Proteintech, 10654–1-AP), anti-HK2 (Proteintech, 22029–1-AP), anti-PKM2 (Proteintech, 60268–1-Ig), anti-P62 (Affinity Biosciences, AF5384), anti-LC3B (Affinity Biosciences, AF5402), anti-ATG5 (Santa Cruz Biotechnology, sc-133158), anti-ATG12 (Santa Cruz Biotechnology, sc-271688), anti-8-oxoguanine (o8G) (Abcam, ab206461 and Sigma, MAB3560), anti-AUF1 (Abcam, ab259895), anti-Tubulin (Servicebio, GB11017) and anti-beta Actin (Servicebio, GB15003) antibodies. The secondary antibodies used were as follows: anti-mouse IgG (Proteintech, SA00001-1), anti-mouse IgG (Cell Signaling Technology, 4408S), anti-rabbit IgG (Cell Signaling Technology, 7074S), and anti-rabbit IgG (Cell Signaling Technology, 8890S).

TRAP

The circPLCE1-MS2 fusion expression vector was constructed, and TRAP experiments were carried out using a TRAP kit (BersinBio, Bes5106). For cell transfection, A549 cells (2×10^7 cells/group) were first prepared, and cell transfection was performed using a Lipofectamine™ 3000 transfection kit (Invitrogen, L3000015). The cells in the negative control group were cotransfected with the MS2 plasmid and MS2-GST plasmid, and the cells in the experimental group were cotransfected with the MS2-circPLCE1 plasmid and MS2-GST plasmid. For cell lysis, cell lysis buffer was prepared according to the manufacturer's instructions, and the cells were lysed on ice for 10 min, subsequently collected into enzyme-free EP tubes and centrifuged at 10,000×*g* for 15 min at 4 °C. Then, 100 μl of the supernatant was separately labelled as input protein. For immunoprecipitation, GSH magnetic beads were activated according to the manufacturer's instructions and subsequently added to each group of cell lysates, and the mixtures were incubated for 3 h at 4 °C with gentle rotation. Subsequently, protein elution buffer was added for RBP collection, and polyacrylamide gel electrophoresis (PAGE)-silver staining and MS analysis were carried out.

RIP

A RIP kit (IEMed, IEMed-K303) was used to conduct RIP experiments to detect the direct binding of circPLCE1 to proteins. Antibody-protein A/G beads were prepared as follows: protein A/G beads were separated into 2 groups, and 2 μg of the target antibody (anti-HSC70, Proteintech, 10654–1-AP) (anti-AUF1, Abcam, ab259895) was added to one group (IP group), and 2 μg of IgG was added to the other group (IgG group). For cell lysis, 1×10^7 cells were detached, centrifuged, collected, and lysed at room temperature for 20 min according to the manufacturer's instructions. For IP, 0.4 ml of the cell lysate was added to the IP group, 0.4 ml was added to the IgG group, and the remaining 0.2 ml was used for the input group. The samples were placed on a vertical mixer for IP for 1 h. Subsequently, RNA was recovered; circPLCE1 enrichment in each group was evaluated via RT–qPCR, and agarose gel electrophoresis was carried out on the basis of the qPCR products.

CLIP

A CLIP kit (BersinBio, Bes3014) was used to conduct the CLIP assays. The circPLCE1 truncation primers were designed with a length of 50 bp (circPLCE1 truncation primers and sequence are shown in Supplementary Table 2), and reverse primers were designed with a plus-tailed universal primer (PCR Reverse Primer). The cells were incubated in medium containing 10% FBS and 100 μM 4-thiouracil (Sigma, T4509) for 16 h, and subsequent experiments were carried out. Antibody–protein A/G beads were prepared as follows: 2 μg of the target antibody and 2 μg of IgG were added to the protein A/G beads in the IP and IgG groups, respectively, and the samples were incubated in a vertical mixer. For UV cross-linking, 3×10^7 cells were placed on ice for UV cross-linking at 365 nm for 10 min to enhance the binding between proteins and RNA molecules. For cell lysis, after UV cross-linking, 1×cell lysis buffer was added to the cells, which were subsequently lysed on ice for 10 min. Immunoprecipitation was then conducted, followed by protein digestion and RNA extraction to evaluate circPLCE1 enrichment via qPCR.

MeRIP

A MeRIP kit (IEMed, IEMed-K305) was used to carry out the MeRIP assay. For RNA extraction, 1×10^7 cells were prepared and lysed using TRIzol reagent, total cellular RNA was extracted, and 50 μg of RNA was sonicated and fragmented for subsequent assays. Antibody–protein A/G beads were prepared as follows: protein A/G beads were divided into 2 tubes for the IP group and the IgG group, and 2 μg of the target antibody and 2 μg of IgG, respectively, were added to the tubes. For immunoprecipitation, 10 μg of RNA (input) was stored temporarily at −20 °C. The remaining RNA was mixed with 400 μl of MeRIP buffer, divided equally into the IP and IgG tubes, and placed in a vertical mixer for incubation at room temperature for 1 h. Subsequently, RNA elution was performed, qPCR was performed to measure circPLCE1 expression in each group, and agarose gel electrophoresis was performed using the qPCR products.

Co-IP

A Co-IP Kit (BersinBio, Bes3011) was used to conduct Co-IP assays to detect protein–protein interactions. Antibody–protein A/G beads were prepared as follows: protein A/G beads were divided into 2 tubes (the IP group and IgG group), and 2 μg of the target antibody and 2 μg of IgG, respectively, were added to the tubes for 30 min of incubation at room temperature. For protein extraction, 2×10^7 cells were prepared, detached and centrifuged for collection. The cell lysis buffer was prepared according to the manufacturer's instructions, the cells were lysed on ice, and the supernatant was collected by centrifugation at 12,000×g for 15 min. For immunoprecipitation, 100 μl of the supernatant was labelled as the input; 600 μl was added to the IP tube, and 600 μl was added to the IgG tube. The mixtures were incubated with shaking on a vertical mixer for 1 h. For elution, the protein samples were eluted with western blot (WB) elution buffer, and the supernatant was collected for PAGE followed by western blotting.

IF analysis

The cells (1×10^5 cells/well) were seeded into 12-well plates containing microscope cover glasses. After the cells had adhered to the plates, 4% PFA was used to fix the cells, blocking buffer (1×PBS/5% FBS/0.3 Triton XTM-100) was added, and the cells were blocked for 1 h at room temperature. Antibody dilution buffer (1×PBS/1% BSA/0.3% Triton XTM-100) was prepared, the primary antibody was added, and the mixture was incubated overnight at 4 °C with shaking. The cells were washed with 1×PBS 3 times and incubated with a fluorescently labelled secondary antibody at room temperature in the dark for 1.5 h. Fluorescence images were acquired using an LSM800 confocal microscope (Zeiss, Oberkochen, Germany) after washing with 1×PBS.

Monodansylcadaverine (MDC) assay for measuring cellular autophagy

The Autophagy Staining Assay Kit with MDC (Beyotime, C3018S) was used to evaluate the level of cellular autophagy. A549 cells were seeded in 6-well plates and transfected for 48 h, and subsequent assays were carried out. The medium was discarded, and autophagy was induced by adding 1 ml of Earle's balanced salt solution (EBSS) per well and incubating at 37 °C for 1 h. The 1×MDC working solution was prepared at an MDC:1×Assay Buffer ratio of 1:1000. Then, 1 ml of 1×MDC working solution was added to each well, and the plates were incubated at 37 °C for 30 min in the dark. The cells were washed well with 1×assay buffer, and an LSM800 confocal microscope (Zeiss, Oberkochen, Germany) was used for fluorescence imaging.

CYTO-ID detection of autophagy

CYTO-ID Autophagy Detection Kit 2.0 (Enzo Life Sciences, ENZ-KIT175) was used to detect cellular autophagy. A549 cells were seeded in 6-well plates and transfected for 48 h before subsequent assays were carried out. For flow cytometric analysis, the cells were detached, collected via centrifugation, washed with PBS and resuspended in 250 μl of 1×assay buffer. CYTO-ID staining solution (1 μl CYTO-ID/1 ml 1×Assay Buffer/5% FBS) was prepared, and the cells were

incubated with this solution at 37 °C in the dark for 30 min. Cellular autophagy was detected with a CytoFLEX flow cytometer (Beckman Coulter) after resuspension and washing of the cells with 1 × Assay Buffer. For fluorescence microscopy, A549 cells were seeded in 12-well plates containing microscope cover glasses and transfected for 48 h before subsequent experiments were carried out. CYTO-ID staining solution (2 μl CYTO-ID/1 ml 1 × Assay Buffer/5% FBS) was prepared, 1 × Assay Buffer was used to wash the cells, and then CYTO-ID staining solution was added to the cells for 30 min of incubation at 37 °C in the dark. Fluorescence imaging was carried out on an LSM800 confocal microscope (Zeiss, Oberkochen, Germany).

RNA stability assay

RNA stability was assessed after ActD (MedChemExpress, HY-17559) treatment of the cells. The cells were seeded in 6-well plates (3×10^6 cells/well); when the cells were approximately 90% confluent, ActD working solution (ActD diluted to 2 μg/ml in medium containing 10% FBS) was added. Total RNA was extracted using TRIzol at 0 h, 4 h, 8 h, 12 h and 24 h. Subsequently, qPCR was performed to measure gene expression and thus analyse RNA stability.

Protein stability assay

Protein stability was evaluated using cycloheximide (CHX) (MedChemExpress, HY-12320). The cells were seeded into six-well plates (3×10^6 cells/well), plasmid transfection was performed when the cell confluence reached 70–80%, and the culture was continued for 48 h. Working solution containing 50 μg/mL CHX was prepared with medium containing 10% FBS; 2 ml of CHX working solution was added to each well, and the proteins were harvested at 0 h, 4 h, 8 h and 12 h. PAGE followed by western blotting was performed to measure protein expression.

Proteasome inhibition assay

Protein expression levels were measured after inhibition of the proteasome with MG132 (MedChemExpress, HY-13259). The cells were seeded into six-well plates (3×10^6 cells/well), plasmid transfection was performed when the cell confluence reached 70–80%, and the culture was continued for 48 h. A working solution containing 100 nM MG132 was prepared with medium supplemented with 10% FBS; 2 ml of medium was added to each well, and the proteins were harvested at 0 h and 24 h. Subsequently, PAGE followed by western blotting was carried out to detect protein expression.

Induction of CMA

For the induction of CMA by starvation, the cells were seeded into six-well plates (3×10^6 cells/well), and CMA was induced via starvation in F-12K medium supplemented with 0.5% FBS. Proteins were harvested at 16 h and 24 h, and PAGE followed by western blotting was carried out to measure protein expression. For treatment with the CMA activator, A549 cells were seeded into six-well plates (3×10^6 cells/well); CMA activity was induced by treatment with 10 μM and 20 μM AR7 (MedChemExpress, HY-101106), and proteins were harvested after 24 h. Then, PAGE followed by western blotting was carried out to measure protein expression.

PA-mCherry-KFERQ reporter assay for the detection of CMA activity

CMA activity was visualized via pSIN-PAmCherry-KFERQ-NE (Addgene, 102365). A549 cells were seeded at a density of 2×10^5 in 12-well plates containing microscope cover glasses. After lentiviral packaging, A549 cells were infected with pSIN-PAmCherry-KFERQ-NE lentiviral particles. Protein expression was activated by exposure to 405 nm light-emitting diode (LED) light for 10 min. The cells were incubated at 37 °C for 16 h and fixed with 4% PFA, and the nuclei were stained with DAPI. Fluorescence imaging was performed with an LSM800 confocal microscope (Zeiss, Oberkochen, Germany).

Statistical analysis

In this study, numerical data are expressed as the means ± standard deviations (SDs). Independent samples *t*-tests were used for comparisons of two groups of data that conformed to a normal distribution and whose variance was similar between the groups; Wilcoxon rank–sum tests were used for comparisons between two groups of data that did not conform to a normal distribution. Count data are expressed as the number of cases (percentages), and the chi-square test was used for comparisons between two groups. Pearson correlation analysis was used to assess correlations between variables. Survival analysis was performed via the Kaplan–Meier method. ROC curves were constructed to evaluate the potential diagnostic value of circPLCE1. Statistical analyses were performed via two-sided tests with $\alpha = 0.05$, and differences with $P < 0.05$ were considered statistically significant. All experiments were carried out with at least three biological replicates, and the data shown represent the results of at least three independent experiments.

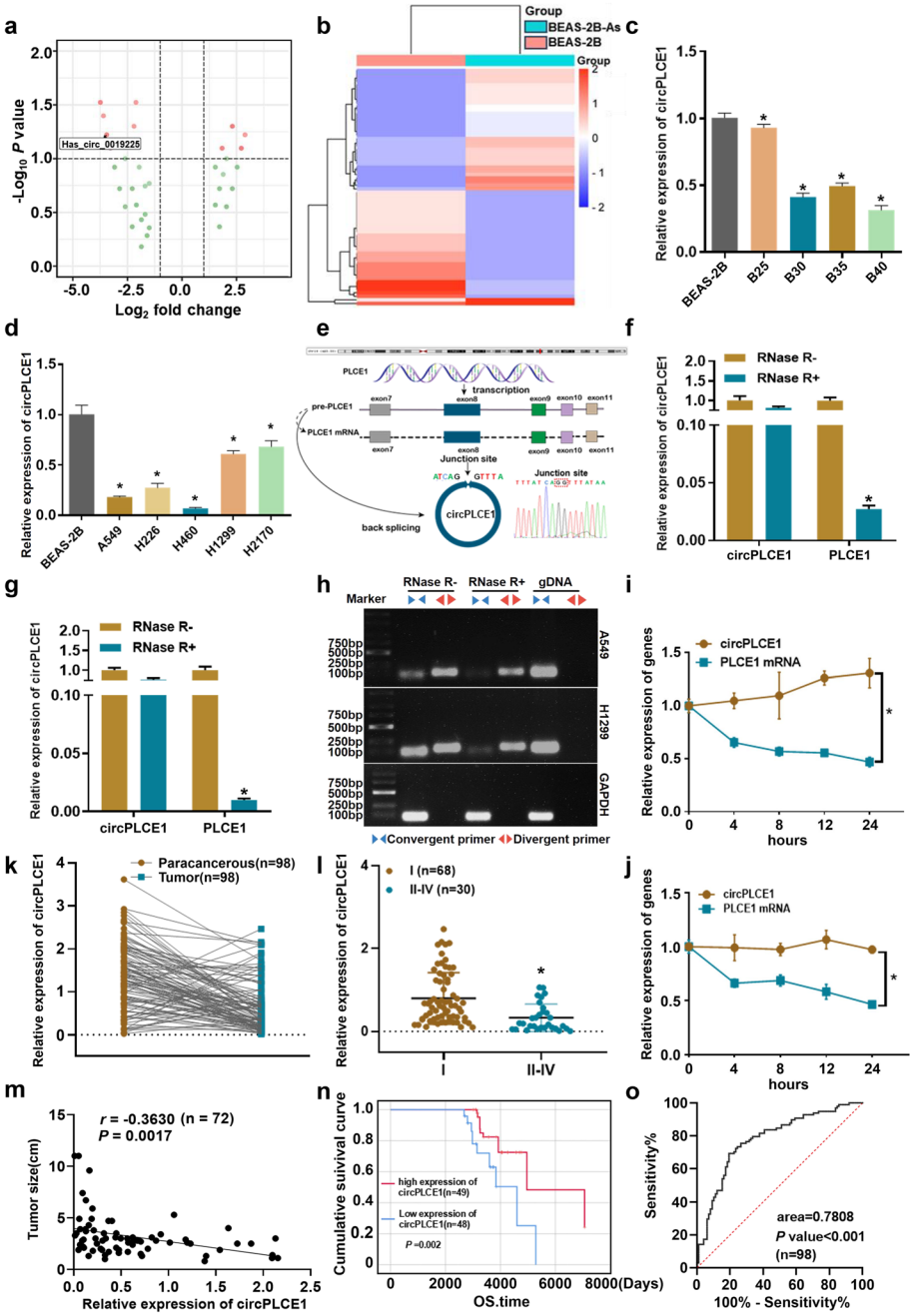

Fig. 1 circPLCE1 is significantly downregulated in lung cancer tissues and cells. **a** Differential expression is indicated in the volcano plot. **b** Heatmap of the differentially expressed circRNAs. **c** qPCR analysis of circPLCE1 expression in different stages of arsenic-induced lung cancer. **d** qPCR analysis of circPLCE1 expression in various lung cancer cell lines (A549, H226, H1299, H460, and H2170). **e.** circPLCE1 gene structure and Sanger sequencing results. **f** A549 cells were treated with RNase R (3 U of RNase R/μg RNA for 10 min), and qPCR was performed to measure the expression levels of circPLCE1 and PLCE1 mRNAs. **g** H1299 cells were treated with RNase R (3 U of RNase R/μg RNA for 10 min), and qPCR was performed to measure the expression levels of circPLCE1 and PLCE1 mRNAs. **h** Agarose gel electropherogram using convergent and divergent primers. **i** A549 cells were treated with 2 μg/ml ActD, and qPCR was performed to measure the expression levels of circPLCE1 and PLCE1 mRNAs. **j** H1299 cells were treated with 2 μg/ml ActD, and qPCR was performed to measure the expression levels of circPLCE1 and PLCE1 mRNAs. **k** qPCR analysis of circPLCE1 expression in lung cancer and paracancerous tissues. **l** circPLCE1 expression in tissue samples of lung cancer at different pathological stages. **m** Correlation analysis between circPLCE1 expression and tumour size (tumour size is expressed as the longest diameter of the tumour). **n** Survival analysis based on circPLCE1 expression (OS time indicates overall survival time). **o** ROC analysis based on circPLCE1 expression

Results

circPLCE1 is significantly downregulated in lung cancer tissues and cells

In previous work, we used sodium arsenite to induce the malignant transformation of human bronchial mucosal epithelial cells (BEAS-2B-As) [18]. High-throughput sequencing of BEAS-2B cells and a BEAS-2B cell model of arsenic-induced malignant transformation was performed to generate differential circRNA expression profiles (Fig. 1a and b, Supplementary Table 1). The differentially expressed circRNAs with "log2 FC > 2" were screened for clustering analysis. The clustering method was "complete", and the distance method was "Euclidean" (Fig. 1b). The circRNA circPLCE1 (hsa_circ_0019225), which is significantly downregulated in cells with arsenic-induced malignant transformation, attracted our attention (Fig. 1c). We found via qPCR that circPLCE1 was significantly downregulated in different lung cancer cell lines compared to BEAS-2B cells (Fig. 1d). Therefore, we selected the non-small cell lung adenocarcinoma cell lines with the most significant downregulation, A549 and H1299, for the follow-up study. The UCSC Genome Browser (http://genome.ucsc.edu/) revealed that circPLCE1 is formed by alternative splicing of exon 8 of PLCE1 on chromosome 10, and its back-splice junction site was identified via Sanger sequencing (Fig. 1e). We subsequently designed divergent primers and convergent primers based on the circPLCE1 splice site (Supplementary Table 2). Total RNA was extracted from A549 and H1299 cells and treated with a linear RNA exoribonuclease (RNase R) for ten minutes to degrade linear RNA. qPCR was subsequently performed and revealed that PLCE1 mRNA was not resistant to RNase R digestion, whereas circPLCE1 was resistant to RNase R digestion (Fig. 1f and g). Agarose gel electrophoresis was performed on the PCR products (Fig. 1h), the results revealed that RNase R degraded the linear products but did not degrade circPLCE1. Subsequently, an RNA stability assay was conducted in A549 and H1299 cells. Actinomycin D (ActD) working solution (2 μg/ml) was added, and the results revealed that circPLCE1 had a longer half-life and greater stability than did homologous linear mRNAs (Fig. 1i and j). These results confirmed that circPLCE1 has a circular structure.

To analyse clinical associations, we assessed the expression level of circPLCE1 in 98 pairs of lung cancer and paracancerous tissues (Supplementary Table 3). circPLCE1 expression was significantly lower in lung cancer tissues than in paracancerous tissues (Fig. 1k). Moreover, circPLCE1 expression was significantly lower in stage II-IV lung cancer tissues than in stage I lung cancer tissues (Fig. 1l). In-depth clinical correlation analysis revealed that the expression level of circPLCE1 in lung cancer tissues was negatively correlated with tumour size ($r = -0.3630$, $P = 0.0017$) (Fig. 1m). Patients with low circPLCE1 expression had poorer overall survival than those with high circPLCE1 expression did, as determined by Kaplan–Meier survival analysis (Fig. 1n). Receiver operating characteristic (ROC) analysis revealed that the area under the curve (AUC) was 0.7808 ($P < 0.001$) (Fig. 1o), indicating that circPLCE1 has potential value as a prognostic biomarker for lung cancer.

circPLCE1 o8G modifications

With in-depth research on RNA modifications, the important roles of the o8G modification in regulating the fate of RNA molecules and in tumorigenesis and tumour progression have been revealed [24–27]. To explore that o8G modification occurs on circPLCE1, we conducted methylated RNA immunoprecipitation (MeRIP) experiments using an o8G modification-specific antibody, and the results revealed that circPLCE1 was significantly enriched with the anti-o8G antibody, suggesting that o8G modification can occur on circPLCE1 (Fig. 2a and b). To further confirm the o8G modification region of circPLCE1, we designed primers to amplify the circPLCE1 truncations in crosslinking immunoprecipitation (CLIP) experiments. These experiments revealed that the o8G modification is predominantly located in the 10th region of circPLCE1 (Fig. 2c and d). It has been shown that o8G modification occurs via ROS attack on guanine bases in RNA, but whether ROS can induce o8G modification of circRNAs is unknown [42–45]. To explore the o8G modification of circPLCE1 in depth, we used a concentration gradient of H_2O_2 and N-acetylcysteine (NAC) to measure intracellular ROS levels on the basis of previous reports. Finally, a H_2O_2 concentration of 200 μM (Fig. 2e and f) and an NAC concentration of 2 mM (Fig. 2g and h) were selected for the subsequent studies. We then carried out IF experiments and found that H_2O_2 increased but NAC decreased the intracellular o8G modification level (Fig. 2i and j), indicating that the level of o8G modification is positively correlated with the level of intracellular ROS. Therefore, we treated A549 cells with H_2O_2 and carried out MeRIP experiments, we found that circPLCE1 o8G modification is increased in the H_2O_2-treated group, suggesting that ROS can induce o8G modification of circPLCE1 (Fig. 2k and l).

ROS attack of guanine bases in an RNA can promote degradation of the RNA via a variety of mechanisms, allowing RNA quality control [46, 47]. Therefore, we carried out an RNA stability assay to assess the molecular

fate of circPLCE1 after o8G modification. The ROS-induced o8G modification resulted in a shorter half-life and reduced the stability of circPLCE1 (Fig. 2m). It has been shown that AUF1 preferentially recognizes o8G modifications in RNA, thereby affecting RNA stability [30]. To further explore whether AUF1 can act as a reader of the circRNA o8G modification and thus regulate the stability of circPLCE1, we carried out RIP experiments. The results revealed that circPLCE1 can directly bind to AUF1 and that AUF1 enrichment increases with increasing o8G modification levels, suggesting that AUF1 specifically recognizes circPLCE1 o8G modifications (Fig. 2n and o). We then designed siRNAs targeting AUF1 to conduct an RNA stability assay using these siRNAs. When AUF1 silencing was combined with H_2O_2 treatment, the results revealed that AUF1 silencing reversed the decrease in circPLCE1 stability caused by o8G modification (Fig. 2p). These results suggest that ROS increase the level of circPLCE1 o8G modification and that AUF1 can act as a reader of o8G modification to mediate decreases in circPLCE1 stability and expression.

circPLCE1 significantly inhibits lung cancer progression in vitro

The functions of circPLCE1-targeted RBPs (Supplementary Fig. 1a) and mRNAs (Supplementary Fig. 1b) were predicted via KEGG enrichment analysis; the results revealed that circPLCE1 is closely related to multiple tumour-associated pathways, suggesting that circPLCE1 may play a role in lung cancer progression. Therefore, to explore the biological function of circPLCE1 in lung cancer, we designed circPLCE1-specific siRNAs and used the pcircRNA 2.2 (Supplementary Fig. 1c) and V53B plv-Puro-circRNA (Supplementary Fig. 1d) vectors to construct plasmids for transient and stable overexpression of circPLCE1. qPCR analysis revealed that the efficiency of transient silencing and overexpression of circPLCE1 was good (Supplementary Fig. 1e) and that silencing/overexpression of circPLCE1 did not affect the mRNA level of its homologous linear product PLCE1 (Supplementary Fig. 1f), indicating that systems for the silencing and overexpression of circPLCE1 were successfully established. We subsequently carried out a series of functional experiments to explore the biological functions of circPLCE1 in vitro in terms of cell proliferation, cell viability, cell cycle progression, apoptosis and migration. First, an EdU incorporation assay was carried out after circPLCE1 was silenced and overexpressed in the lung cancer cell lines A549 and H1299, and the results revealed that circPLCE1 silencing significantly promoted the proliferation of these lung cancer cell lines while circPLCE1 overexpression significantly inhibited proliferation (Fig. 3a and b). A CCK-8 assay was subsequently performed, and the results revealed that circPLCE1 silencing significantly increased the viability of these lung cancer cell lines while circPLCE1 overexpression significantly decreased viability (Fig. 3c). To explore the effects of circPLCE1 on apoptosis and the cell cycle, we performed flow cytometry. Apoptosis was suppressed by circPLCE1 silencing but promoted by circPLCE1 overexpression (Fig. 3d and e); cell cycle progression was accelerated after circPLCE1 was silenced and slowed after circPLCE1 was overexpressed (Fig. 3f and g). With disease progression, metastasis to various organs often occurs in patients with advanced lung cancer, posing a serious threat to patients' lives and health. Therefore, we conducted Transwell assays and wound healing to explore whether circPLCE1 plays a role in lung cancer migration and found that circPLCE1 suppresses the migration of lung cancer cells (Fig. 3h and i, Supplementary Fig. 1 g and h). Taken together, these results suggest that circPLCE1 can significantly inhibit lung cancer progression in vitro.

circPLCE1 significantly inhibits lung cancer progression in vivo

We clarified that circPLCE1 has a biological function in significantly inhibiting lung cancer progression in vitro. To explore whether circPLCE1 also inhibits lung cancer progression in vivo, we established a subcutaneous xenograft model in nude mice. A549 cells with stable circPLCE1 overexpression were generated via lentiviral transduction and selected by puromycin screening (Fig. 4a and b). Nude mice were maintained under specific pathogen-free (SPF) conditions for 1 week, after which the circPLCE1 vector or circPLCE1 OE A549 cells were injected subcutaneously into the right dorsal surface of the nude mice. The survival status of the nude mice was monitored at three-day intervals, and the mouse body weights and tumour diameters were measured. Compared with those in the control group, the tumours in the stable circPLCE1 overexpression group were smaller (Fig. 4c) and grew more slowly (Fig. 4d). The nude mice were sacrificed 21 days after tumour formation, and the tumours were excised for observation and weighing. Compared with those in the control group, the tumours in the circPLCE1-overexpressing group were smaller in size (Fig. 4e) and lighter in weight (Fig. 4f). Subsequently, immunohistochemistry was performed to detect changes in the expression of proteins related to lung cancer progression, including a proliferation-related protein (Ki67), an apoptosis-related protein (BCL2), and a migration-related protein (RhoA), in tumours from nude mice. Protein expression was quantified and analysed, and compared with those in the control group, the tumours in the stable circPLCE1

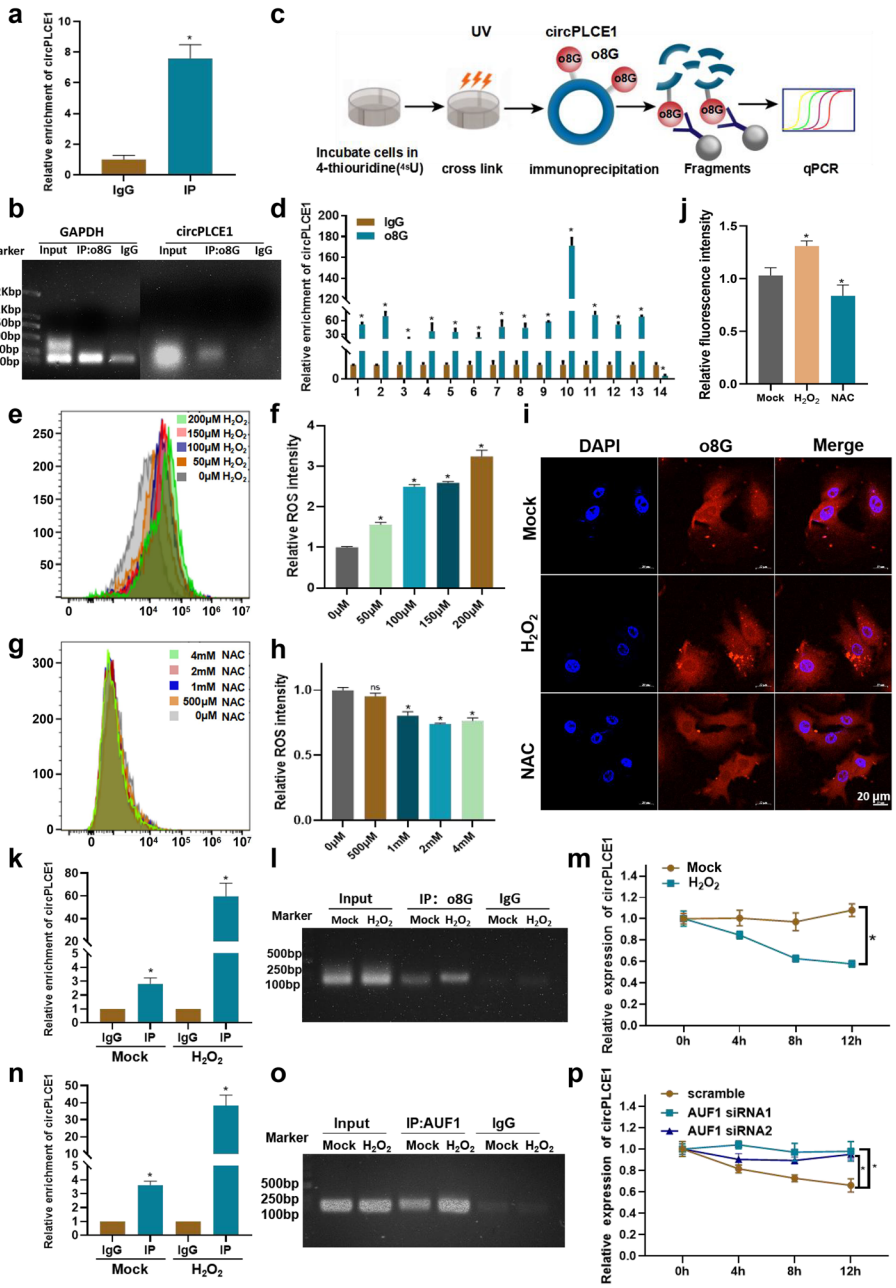

Fig. 2 circPLCE1 o8G modification. **a** MeRIP assay using A549 cells and MeRIP–qPCR analysis of the circPLCE1 o8G modification. **b** MeRIP products were subjected to agarose gel electrophoresis. **c** Schematic diagram of the CLIP experiment. **d** CLIP assay using A549 cells and CLIP–qPCR analysis of the o8G modification region in circPLCE1. **e** Intracellular ROS detection in A549 cells treated with different concentrations H_2O_2. **f** Statistical analysis of ROS levels after treatment with different concentrations of H_2O_2. **g** Intracellular ROS detection in A549 cells after treatment with different concentrations of NAC. **h** Statistical analysis of the ROS levels after treatment with different concentrations of NAC. **i** IF staining was carried out in A549 cells to detect o8G modification levels (red fluorescence: o8G modification; blue fluorescence: nucleus) after treatment with 200 μM H_2O_2 and 2 mM NAC. **j** Statistical graphs of the results of the quantitative analysis of the IF results. **k** MeRIP assay using A549 cells and MeRIP–qPCR analysis of circPLCE1 o8G modification after treatment with 200 μM H_2O_2. **l** The MeRIP products were subjected to agarose gel electrophoresis after treatment with 200 μM H_2O_2. **m** An RNA stabilization assay was carried out after treatment of A549 cells with 200 μM H_2O_2. **n** After A549 cells were treated with 200 μM H_2O_2, a RIP–qPCR assay was performed to detect the interaction between circPLCE1 and AUF1. **o** The RIP products were subjected to agarose gel electrophoresis after treatment with 200 μM H_2O_2. **p** An RNA stabilization assay was carried out after treatment of A549 cells with 200 μM H_2O_2 and AUF1 knockdown

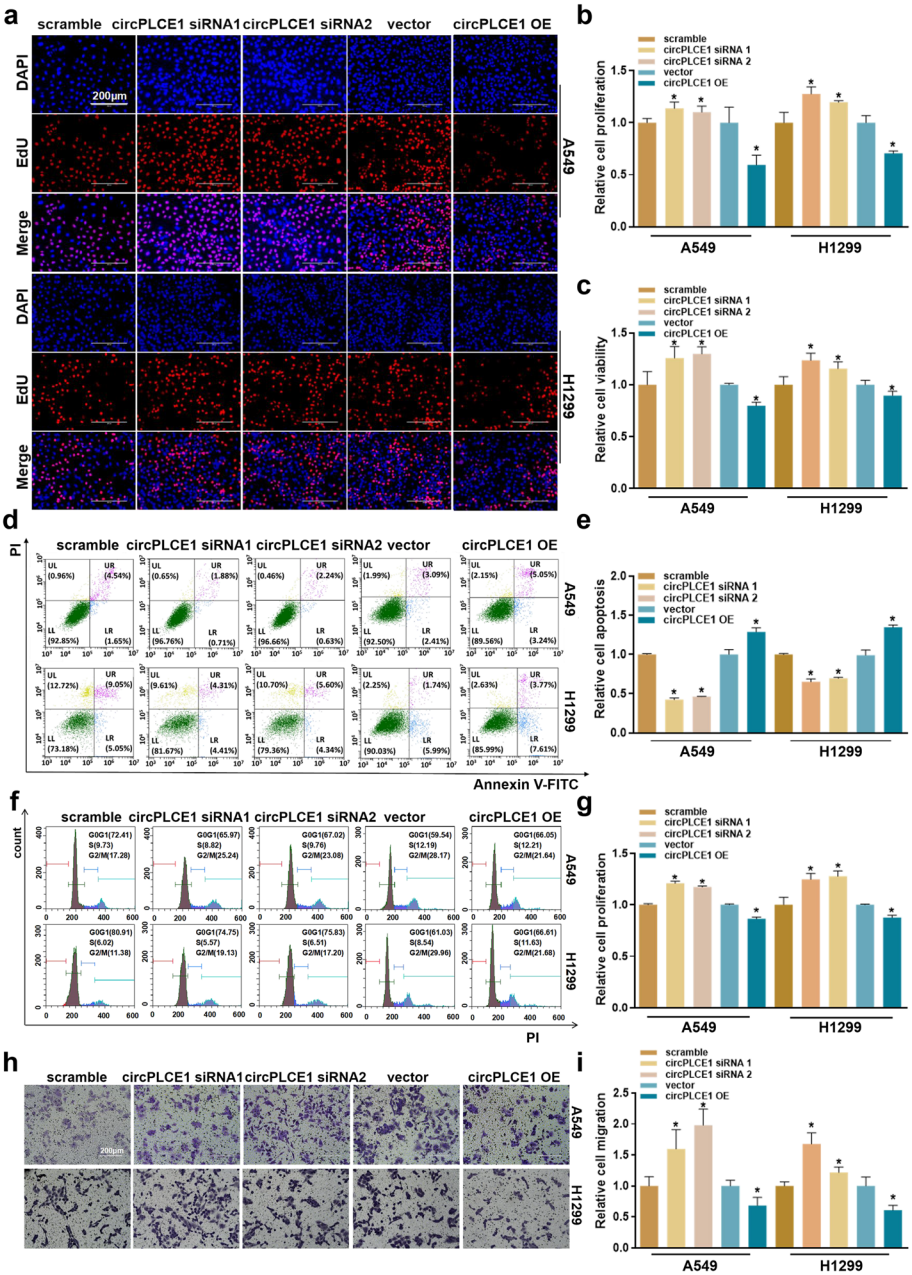

Fig. 3 circPLCE1 significantly inhibits lung cancer progression in vitro. Silencing/overexpression of circPLCE1 in A549 and H1299 cells. **a** EdU incorporation assay of cell proliferation after circPLCE1 silencing/overexpression. **b** Statistical analysis of the EdU incorporation assay results. **c** CCK-8 assay of cell viability after circPLCE1 silencing/overexpression. **d** Flow cytometry analysis of apoptosis after circPLCE1 silencing/overexpression. **e** Statistical analysis of the flow cytometric apoptosis assay results. **f** Analysis of the cell cycle distribution after circPLCE1 silencing/overexpression via flow cytometry. **g** Statistical analysis of the flow cytometric cell cycle analysis results. **h** Transwell migration assay after circPLCE1 silencing/overexpression. **i** Statistical analysis of the results of the Transwell assay

overexpression group presented lower expression of Ki67 (Fig. 4g and j), BCL2 (Fig. 4h and j), and Rho A (Fig. 4i and j). These results indicate that circPLCE1 can significantly inhibit lung cancer progression in vivo.

circPLCE1 targets the HSC70 protein and regulates its ubiquitination

Since the subcellular localization of a gene is closely related to its molecular mechanism, we carried out nuclear–cytoplasmic separation and fluorescence in situ hybridization (FISH), which revealed that circPLCE1

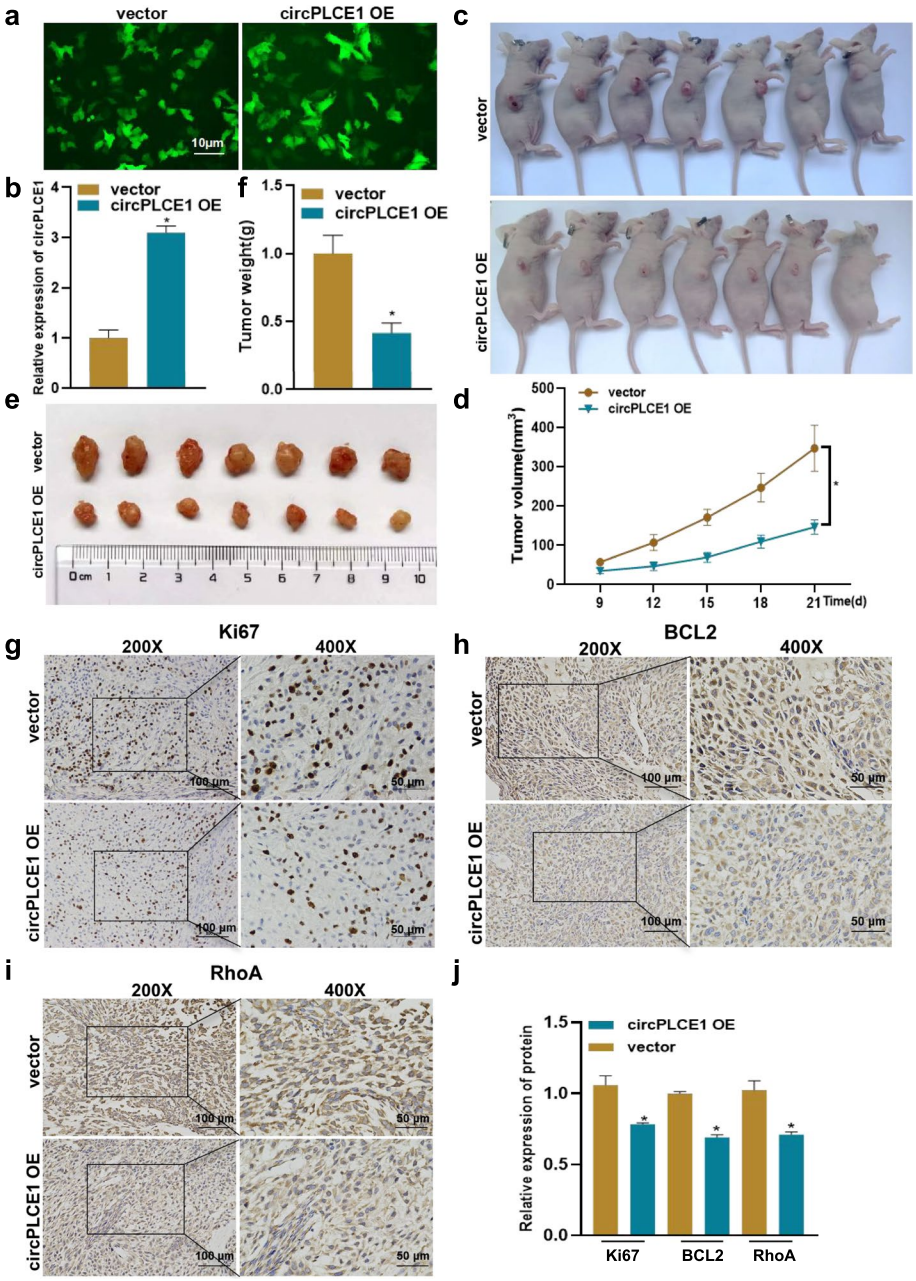

Fig. 4 circPLCE1 significantly inhibits lung cancer progression in vivo. **a** Fluorescence visualization after lentiviral packaging. **b** Stable overexpression efficiency of circPLCE1. **c** Cells stably overexpressing circPLCE1 and the corresponding control cells were injected subcutaneously into the right dorsal surface of female nude mice at 4 weeks of age, and the ability of the cells to form subcutaneous tumours was observed after 21 days. **d** Tumour growth curves for each group of nude mice during rearing. **e** Excision of the tumours for photographic documentation. **f** Weights of the tumours from the nude mice. **g** Immunohistochemical analysis of Ki67 expression. **h** Immunohistochemical analysis of BCL2 expression. **i** Immunohistochemical analysis of RhoA expression. **j** Quantitative analysis of the immunohistochemistry results

was expressed in both the cytoplasm and nucleus but was localized mainly in the cytoplasm (Fig. 5a and b). Numerous studies have revealed that direct binding to proteins is an important mechanism by which circRNAs perform their functions [48–50]. Therefore, we constructed a circPLCE1-MS2 fusion expression vector and performed tagged RNA affinity purification (TRAP)-mass spectrometry (MS) to enrich and identify proteins that directly bind to circPLCE1 (Supplementary Fig. 2a, Supplementary Table 4). Screening for proteins

with RNA-binding ability with the catRAPID (tartaglialab.com) in the MS data (Supplementary Fig. 2b) and KEGG enrichment analysis algorithm revealed that circPLCE1 may be involved in multiple tumour-related pathways, such as endoplasmic reticulum protein processing (Fig. 5c). We performed an M-versus-A plot (MA plot) analysis and selected HSC70, which had the highest binding score in this pathway, for in-depth exploration (Supplementary Fig. 2c). The RIP assay further revealed that circPLCE1 can directly bind to the HSC70 protein (Fig. 5d and e). We subsequently found via western blot (WB) analysis that circPLCE1 negatively regulates HSC70 protein expression (Fig. 5 f and g). Immunohistochemical analysis of HSC70 expression also revealed that HSC70 expression was significantly decreased in nude mouse tumours with stable overexpression of circPLCE1 (Fig. 5h, Supplementary Fig. 2d). Proteins were extracted from the nude mouse tumours, and WB analysis revealed that the HSC70 protein level in the nude mouse tumours was reduced after stable overexpression of circPLCE1 (Fig. 5i). Analysis of the TCGA database (https://xena.ucsc.edu) revealed that HSC70 was significantly overexpressed in lung cancer tissue samples compared to normal tissues samples (Supplementary Fig. 2e and f) and that patients with high HSC70 expression have a lower survival rate (Fig. 5j).

To further explore how circPLCE1 regulates HSC70, we measured HSC70 expression via qPCR and found that alteration of circPLCE1 expression did not affect HSC70 mRNA expression (Supplementary Fig. 2 g). Therefore, we speculated that circPLCE1 may affect HSC70 expression at the protein level. First, we treated A549 cells with CHX, and after protein synthesis was inhibited, we found that circPLCE1 significantly shortened the HSC70 half-life (Fig. 5k and l). Since the ubiquitin proteasome pathway is the major degradation pathway for proteins, we focused on the ubiquitination of HSC70. We treated cells with MG132 and found that circPLCE1 failed to alter the protein level of HSC70 upon inhibition of the proteasome (Fig. 5m and n), which also suggests that the regulation of HSC70 protein levels by circPLCE1 occurs via the ubiquitin–proteasome pathway. Combining these results with those of subsequent coimmunoprecipitation (Co-IP) experiments (Fig. 5o), we concluded that circPLCE1 can affect the ubiquitination level of the HSC70 protein and regulate its ubiquitin-mediated degradation. Our previous results indicated that H_2O_2 treatment resulted in increased circPLCE1 o8G modifications and reduced circPLCE1 stability (Fig. 2k-m). AUF1 specifically recognizes the circPLCE1 o8G modification and mediates the decrease in circPLCE1 stability (Fig. 2n-p). To assess whether circPLCE1 regulates HSC70 protein expression through o8G modification, we treated A549 cells with H_2O_2 and knocked down AUF1 at the same time (Supplementary Fig. 2 h). WB analysis revealed that HSC70 protein expression was increased by H_2O_2 treatment (Fig. 5p, Supplementary Fig. 2i), whereas AUF1 knockdown reversed the trend of increased HSC70 protein expression (Fig. 5p, Supplementary Fig. 2i). These results indicate that o8G modification decreases the stability of circPLCE1 and that circPLCE1 can decrease the stability and expression level of HSC70 via direct binding.

circPLCE1 regulates ATG5 protein expression through the CMA pathway

Through a literature review, we found that HSC70 is a key protein for not only endoplasmic reticulum protein processing but also molecular CMA [51]. CMA is a form of selective autophagy that mediates the lysosomal degradation of proteins containing a KFERQ motif via HSC70 [39]. Since circPLCE1 regulates the HSC70 protein level, we hypothesized that circPLCE1 has the potential to regulate the CMA pathway through HSC70. To explore whether circPLCE1 regulates CMA activity, we selected 2 reported CMA substrates (PKM2 and HK2) for subsequent studies [52, 53]. Co-IP experiments in A549 cells revealed that HSC70 interacts with PKM2 (Fig. 6a). IF experiments revealed the intracellular colocalization of HSC70 with PKM2, and the Pearson correlation coefficient was 0.752 (Fig. 6b), suggesting that one of the conditions for being a CMA substrate is bind directly to HSC70. Numerous studies have revealed that CMA can be activated under conditions such as starvation and oxidative stress [54–56]. Thus, we subjected lung cancer cells to serum starvation and found that the expression of HK2 and PKM2 decreased with increasing duration of starvation (specifically at the 16 h and 24 h time points) (Fig. 6c, Supplementary Fig. 3a and b). Subsequently, we treated lung cancer cells with a CMA-specific agonist (AR7), which revealed that the expression of HK2 and PKM2 decreased with increasing concentrations of AR7 (Fig. 6d, Supplementary Fig. 3c and d). Similarly, the expression of HK2 and PKM2 decreased with increasing treatment time (Supplementary Fig. 3e and f). The above results indicated that the expression level of the CMA substrate was related to CMA activity and decreased after CMA activity increased. Next, we silenced and overexpressed circPLCE1 and found that circPLCE1 positively regulated the expression of CMA substrate proteins (HK2 and PKM2) (Fig. 6e, Supplementary Fig. 3 g and h). Immunohistochemistry also revealed that circPLCE1 promoted HK2 and PKM2 protein expression in vivo (Fig. 6f and g, Supplementary Fig. 3i). The above results suggested that circPLCE1 regulates the CMA substrate levels (HK2 and PKM2) both in vitro and in vivo. We subsequently constructed an

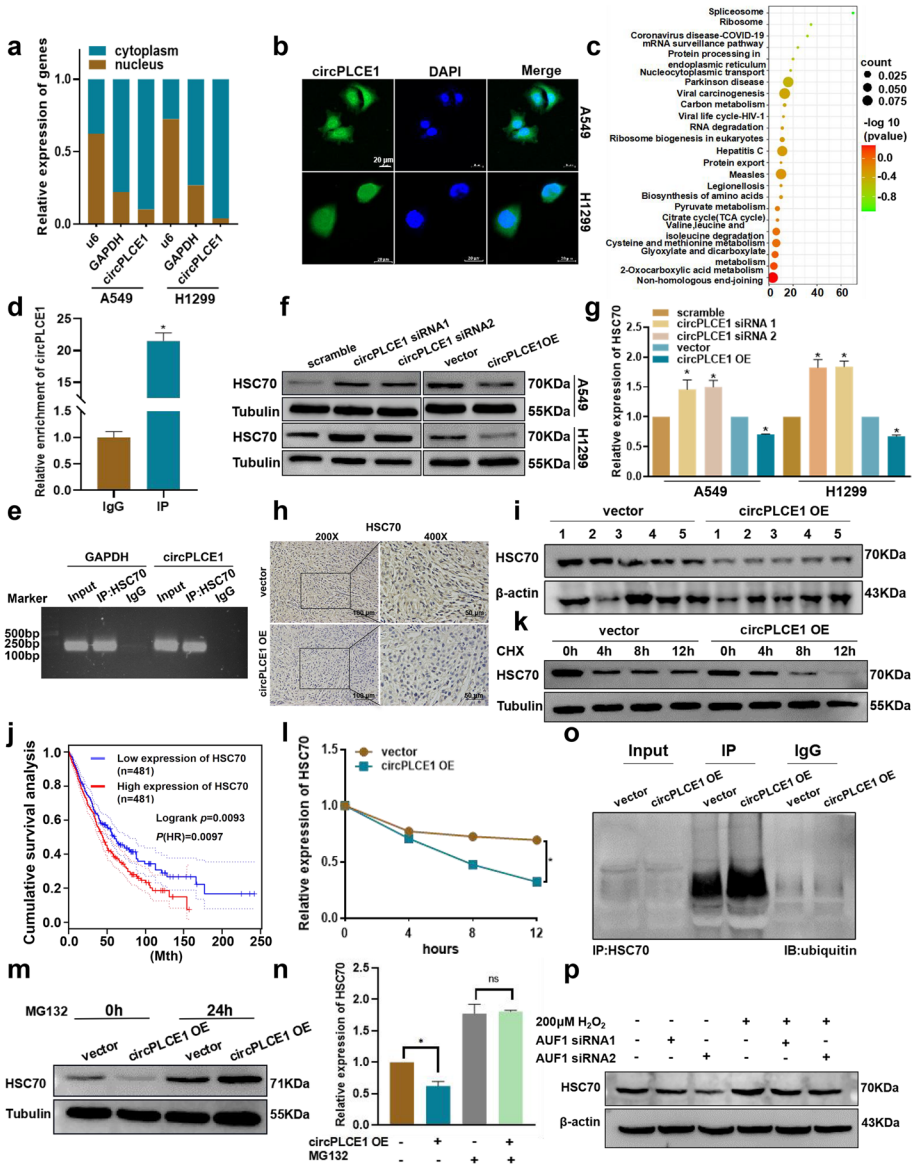

Fig. 5 circPLCE1 targets the HSC70 protein and regulates its ubiquitination. **a** Evaluation of the subcellular localization of circPLCE1 via a nuclear–cytoplasmic separation assay in A549 and H1299 cells. **b** Evaluation of the subcellular localization of circPLCE1 via FISH in A549 and H1299 cells (green fluorescence: circPLCE1; blue fluorescence: nucleus). **c** KEGG enrichment analysis of proteins identified by circPLCE1 TRAP–MS. **d** RIP assay using A549 cells and RIP–qPCR analysis of the direct binding of circPLCE1 to HSC70. **e** The RIP products were subjected to agarose gel electrophoresis. **f** Protein expression levels of HSC70 analysed by WB after circPLCE1 silencing/overexpression in A549 and H1299 cells. **g** Statistical analysis of the HSC70 WB analysis results. **h** Immunohistochemical analysis of HSC70 protein expression in nude mouse subcutaneous tumours. **i** WB analysis of HSC70 expression in nude mouse tumours. **j** Survival analysis on the basis of HSC70 expression (HR, hazard ratio). **k** HSC70 protein stability was analysed by WB after inhibition of protein synthesis by treatment of A549 cells with 50 μg/mL CHX. **l** Statistical analysis of HSC70 protein stability. **m** HSC70 protein expression was analysed by WB after inhibition of the protein proteasome by treatment of A549 cells with 100 nM MG132. **n** Statistical analysis of HSC70 WB data after MG132 treatment. **o** A co-IP assay was carried out in A549 cells to detect the binding of the HSC70 protein to ubiquitin (ubiquitin). **p** WB analysis of HSC70 protein expression levels after 200 μM H_2O_2 treatment combined with AUF1 silencing in A549 cells

HSC70 overexpression plasmid and measured the HSC70 expression level via qPCR (Supplementary Fig. 3j). A549 cells were treated with 20 μM AR7 for 24 h while circPLCE1 was overexpressed, and western blotting was performed. The results revealed that overexpressing circPLCE1 increased the expression level of the CMA substrates HK2 and PKM2. However, the addition of AR7 reversed the increased of HK2 and PKM2 induced by

circPLCE1 overexpression, indicating that circPLCE1 may be related to CMA activity (Fig. 6h, Supplementary Fig. 3 k and l). Subsequently, the overexpression of circPLCE1 in A549 cells was accompanied by the overexpression of HSC70, and WB analysis revealed that the overexpression of circPLCE1 increased the expression levels of the CMA substrates HK2 and PKM2. However, HSC70 overexpression reversed the increase in HK2 and PKM2 expression induced by circPLCE1 overexpression, indicating that circPLCE1 regulates CMA substrates via HSC70 (Fig. 6i, Supplementary Fig. 3 m and n). Further, we used a fusion protein with KFERQ motifs to visualize CMA activity (pSIN-PAmCherry-KFERQ-NE can be used as a defined CMA substrate and can be observed by fluorescence). The number of red fluorescent puncta was significantly reduced after circPLCE1 was overexpressed, and CMA activity was decreased (Fig. 6j, Supplementary Fig. 3o). Taken together, these results indicate that circPLCE1 can regulate CMA activity through HSC70.

It has been shown that CMA is closely related to macroautophagy, but the crosstalk between CMA and macroautophagy has not been elucidated [57]. Thus, we sought to explore whether circPLCE1 can regulate key macroautophagy proteins through the CMA pathway and thus regulate macroautophagy. We initially found via protein interaction prediction (https://cn.string-db.org/) that HSC70 has the potential to interact with key macroautophagy proteins (Supplementary Fig. 4a). Co-IP and IF experiments subsequently revealed that HSC70 can interact with the key protein of macroautophagy (ATG5) (Fig. 6k) and colocalize with it intracellularly, with a Pearson correlation coefficient of 0.776 (Fig. 6l). A query of KFERQ motifs (https://rshine.einsteinmed.edu/) revealed that ATG5 has three KEFRQ motifs (KDVLR, DKVKK, and FRIYQ), suggesting that it may be a potential CMA substrate protein. To further explore whether ATG5 can act as a potential CMA substrate, we subjected lung cancer cells to serum starvation and found that ATG5 protein expression was decreased after starvation (Fig. 6m, Supplementary Fig. 4b). Moreover, after treatment with AR7, the expression of ATG5 decreased along with increasing AR7 concentration (Fig. 6n, Supplementary Fig. 4c). Similarly, ATG5 expression decreased with increasing AR7 treatment time (Supplementary Fig. 4d). To exclude the effect of AR7 on ATG5 mRNA, we treated A549 cells with 10 μM and 20 μM AR7; collected the cells at 0, 16, and 24 h to extract RNA; and then carried out qPCR experiments, which revealed that AR7 did not affect the level of ATG5 mRNA (Supplementary Fig. 4e). These results suggest that ATG5 can act as a CMA substrate. Therefore, we silenced and overexpressed circPLCE1 and assessed the ATG5 expression level via western blotting and found that circPLCE1 promotes ATG5 protein expression (Fig. 6o and p). Immunohistochemistry revealed that stable overexpression of circPLCE1 significantly increased ATG5 expression (Fig. 6q, Supplementary Fig. 4f). A549 cells with circPLCE1 overexpression were treated with 20 μM AR7 for 24 h, and western blotting was carried out. The results revealed that overexpressing circPLCE1 increased the expression level of the CMA substrate ATG5 by inhibiting CMA activity. However, the addition of AR7 reversed the decrease in CMA activity induced by circPLCE1 overexpression, leading to a reduction in ATG5 expression (Fig. 6r, Supplementary Fig. 4 g). Notably, the overexpression of circPLCE1 in A549 cells was accompanied by the overexpression of HSC70, and western blotting revealed that the overexpression of circPLCE1 increased the expression level of the CMA substrate ATG5 by inhibiting CMA activity. However, HSC70 overexpression reversed the increase in ATG5 expression induced by circPLCE1 overexpression (Fig. 6s, Supplementary Fig. 4 h). These results indicate that circPLCE1 can target HSC70 to inhibit CMA activity and increase ATG5 protein expression through the CMA pathway.

circPLCE1 inhibits lung cancer progression by targeting HSC70 and regulates ATG5-dependent macroautophagy via the CMA pathway

These previous results suggest that circPLCE1 inhibition of CMA leads to increased ATG5 expression. Therefore, we further explored whether circPLCE1 can regulate ATG5-dependent macroautophagy and inhibit lung cancer progression. We detected cellular autophagy via flow cytometry after circPLCE1 was silenced or overexpressed and found that circPLCE1 positively regulated macroautophagy (Fig. 7a and b). Detection of cellular autophagy via MDC staining and CYTO-ID staining also revealed that circPLCE1 positively regulated macroautophagy (Fig. 7c and d). WB analysis was performed to assess the expression of ATG12 and autophagy markers (P62 and LC3B), and circPLCE1 was found to positively regulate ATG12 protein expression (Fig. 7e, Supplementary Fig. 5a), negatively regulate P62 protein expression (Fig. 7e, Supplementary Fig. 5b) and positively regulate LC3B protein expression (Fig. 7e, Supplementary Fig. 5c). These findings demonstrated that circPLCE1 can promote macroautophagy in vitro. We subsequently explored whether circPLCE1 can promote macroautophagy in vivo via immunohistochemical analysis of the autophagy markers P62 and LC3B in nude mouse tumours. The expression of P62 was decreased in the nude mouse tumours with stable overexpression of circPLCE1 (Fig. 7f, Supplementary Fig. 5d), and the expression of LC3B was increased in these tumours (Fig. 7g, Supplementary Fig. 5d). WB analysis of proteins extracted from

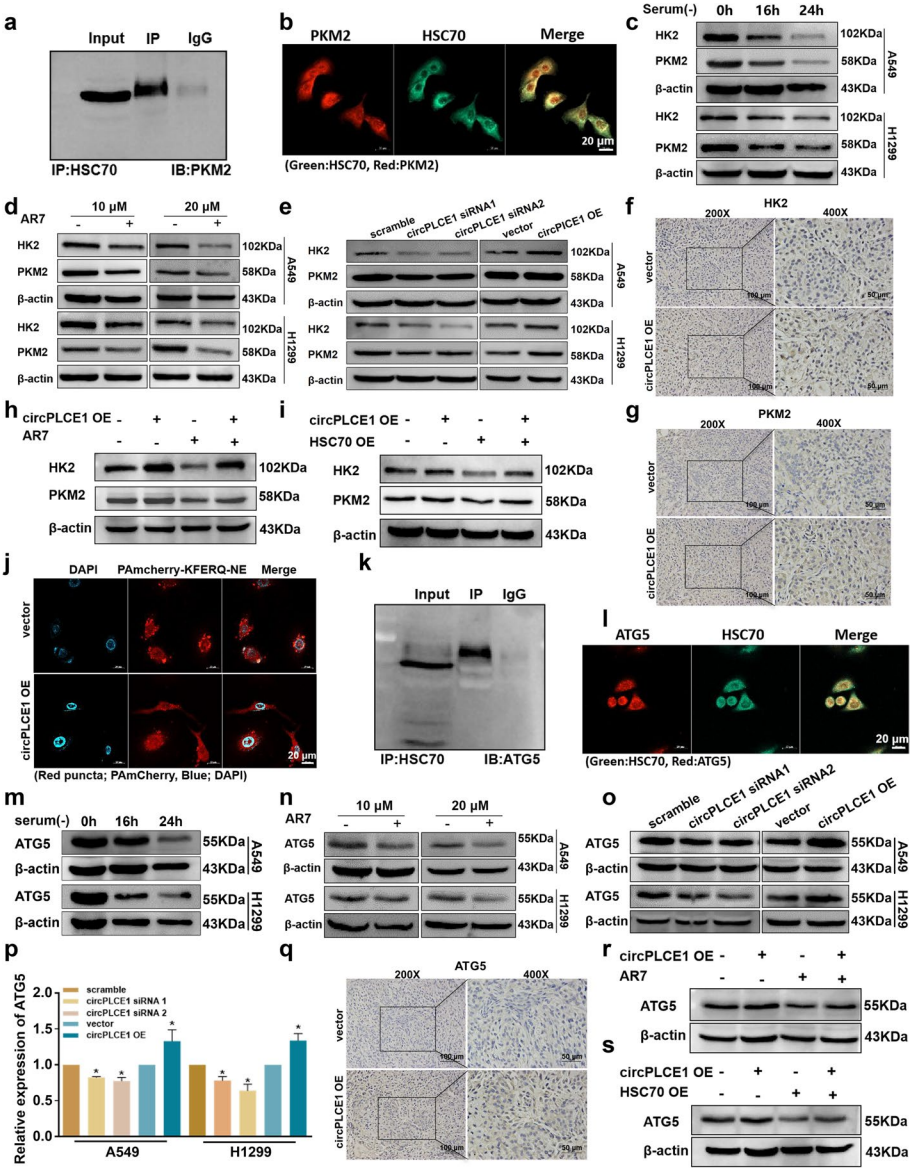

Fig. 6 circPLCE1 regulates ATG5 protein expression through the CMA pathway. **a** A Co-IP assay was carried out in A549 cells to detect the interaction between the HSC70 protein and the PKM2 protein. **b** IF staining was carried out in A549 cells to detect the colocalization of HSC70 and PKM2 (red fluorescence: PKM2; green fluorescence: HSC70; yellow: merged), and Pearson correlation coefficient analysis was performed via Fiji ImageJ. **c** A549 and H1299 cells were serum starved for 16 and 24 h, and WB was carried out to analyse the protein expression levels of HK2 and PKM2. **d** A549 and H1299 cells were treated with 10 μM and 20 μM AR7, and HK2 and PKM2 protein expression levels were detected via WB analysis. **e** WB analysis of HK2 and PKM2 expression levels after circPLCE1 silencing/overexpression. **f** Immunohistochemical analysis of HK2 expression in nude mouse tumours. **g** Immunohistochemical analysis of PKM2 expression in nude mouse tumours. **h** A549 cells were treated with 20 μM AR7 for 24 h, circPLCE1 was overexpressed at the same time, and WB was carried out to detect HK2 and PKM2 protein expression levels. **i** Overexpression of circPLCE1 in A549 cells was accompanied by overexpression of HSC70, and the expression levels of HK2 and PKM2 were analysed by WB analysis. **j** Evaluation of CMA levels in A549 cells with the pSIN-PAmCherry-KFERQ-NE reporter (red puncta: PAmCherry; blue: DAPI). **k** A Co-IP assay was carried out in A549 cells to detect the interaction of the HSC70 protein with the ATG5 protein. **l** IF staining was carried out in A549 cells to detect the colocalization of HSC70 with ATG5 (red fluorescence: ATG5; green fluorescence: HSC70; yellow fluorescence: merged), and Pearson correlation coefficient analysis was performed via Fiji ImageJ. **m** A549 and H1299 cells were serum starved for 16 and 24 h, and WB was carried out to analyse the expression levels of ATG5. **n** A549 and H1299 cells were treated with 10 μM and 20 μM AR7, and ATG5 protein expression levels were detected via WB analysis. **o** WB analysis of ATG5 expression after circPLCE1 silencing/overexpression. **p** Statistical analysis of the ATG5 WB data after circPLCE1 silencing/overexpression. **q** Immunohistochemical analysis of ATG5 expression in nude mouse tumours. **r** A549 cells were treated with 20 μM AR7 for 24 h, circPLCE1 was overexpressed at the same time, and WB was carried out to detect the ATG5 protein expression level. **s** Overexpression of circPLCE1 in A549 cells was accompanied by overexpression of HSC70, and the expression levels of ATG5 were analysed via WB

nude mouse tumours revealed that stable overexpression of circPLCE1 resulted in decreased P62 expression and increased LC3B expression (Supplementary Fig. 5e). These results suggest that circPLCE1 promotes macroautophagy. To explore whether circPLCE1 regulates macroautophagy through ATG5, we designed an ATG5-specific siRNA, and qPCR and WB experiments revealed that silencing ATG5 resulted in decreases in both the ATG5 mRNA and protein expression levels (Supplementary Fig. 5f and g). ATG5 was silenced when circPLCE1 was overexpressed, and macroautophagy was quantitatively analysed via flow cytometry. ATG5 silencing reversed the increase in macroautophagy induced by circPLCE1 overexpression (Fig. 7h, Supplementary Fig. 5 h). The levels of the autophagy markers P62 and LC3B were subsequently assessed by western blotting. Silencing ATG5 reversed the decrease in P62 expression caused by the overexpression of circPLCE1, and reversed the increase in LC3B expression caused by the overexpression of circPLCE1 (Fig. 7i and Supplementary Fig. 5i). The above results revealed that circPLCE1 promotes macroautophagy through an ATG5-dependent pathway.

Many studies have reported the inhibitory role of ATG5-related macroautophagy in lung cancer and other cancers [58–60]. Therefore, to focus on exploring the role of HSC70-mediated CMA downregulation in lung cancer progression, we constructed an HSC70 overexpression plasmid and designed rescue experiments. We overexpressed circPLCE1 simultaneously with HSC70. First, cellular autophagy was quantitatively analysed via flow cytometry, and the results revealed that HSC70 overexpression reversed the increase in macroautophagy induced by circPLCE1 overexpression (Supplementary Fig. 5j and k), the above results suggested that circPLCE1 promotes macroautophagy by targeting HSC70. Subsequently, CCK-8 and EdU incorporation assays were carried out to evaluate cell viability and cell proliferation capacity, respectively. HSC70 overexpression reversed the decreases in cell viability (Fig. 7j) and cell proliferation capacity (Fig. 7k, Supplementary Fig. 5 l) induced by circPLCE1 overexpression. Analysis of apoptosis via flow cytometry revealed that HSC70 overexpression reversed the increase in apoptosis induced by circPLCE1 overexpression (Fig. 7l and 7m). Considering these results collectively, we conclude that circPLCE1 can target HSC70, inhibit CMA activity, and promote ATG5-dependent macroautophagy through the CMA pathway, thereby inhibiting lung cancer progression.

Discussion

Approximately 80% of the sequences in the human genome are transcribed into RNA; of these transcribed sequences, only approximately 2% are mRNAs encoding proteins, and the rest constitute a wide variety of regulatory RNA molecules [61, 62]. In the past 20 years, circRNAs have been considered “by-products” of aberrant splicing and have almost no biological function. With advances in research, important roles of circRNAs in human diseases have been revealed [8, 10, 11]. Studies have revealed that many circRNAs are aberrantly expressed in diverse malignant tumours, including lung, liver, bladder, and oral tumours, and are involved in tumorigenesis and tumour progression [8, 11]. Dysregulation of circRNAs can drive tumorigenesis and tumour progression through a variety of functional mechanisms, making circRNAs effective targets for cancer therapy. We found that circPLCE1, which is sheared from exon 8, is significantly downregulated in lung cancer cells and tissues and correlated with tumour stage and prognosis, suggesting that circPLCE1 may play an important role in lung cancer progression. To date, studies have revealed the role of different isoforms of circPLCE1 in cancer; for example, one circPLCE1 isoform that is formed by the shearing of PLCE1 exon 2 acts as an NF-κB regulator to inhibit the progression of colorectal carcinoma (CRC) by promoting the ubiquitin-dependent degradation of RPS3 and decreasing NF-κB nuclear translocation [63]. Another circPLCE1 isoform formed by the shearing of PLCE1 exons 12 and 13 mediates SRSF2-dependent PLCE1 pre-RNA splicing to promote the malignant progression of colorectal cancer. It has also been reported that circPLCE1 promotes CRC epithelial mesenchymal transition, glycolysis and M2 polarization in tumour-associated macrophages. These findings suggest that the diversity of circRNAs generated due to different alternative splicing patterns leads to a wide range of circRNA biological functions in tumours. Through in vitro and in vivo functional experiments, circPLCE1 was found to inhibit lung cancer cell viability, proliferation, and migration and to promote apoptosis, indicating that circPLCE1 has the biological function of inhibiting lung cancer progression. Our study results are consistent with the role of circPLCE1 as a cancer inhibitor, as previously reported by Liang et al. [63]. However, the biological function of circPLCE1 in lung cancer has not been revealed in previous studies.

In this study, we revealed that ROS can induce circPLCE1 o8G modification. The o8G modification was initially thought to be a product of oxidative damage to DNA, and as research progressed, related studies were extended to RNA. Because it is single-stranded and lacks protection from histones, RNA is more susceptible to ROS-mediated oxidation in vivo than DNA is [64]. o8G modifications are important RNA modifications in eukaryotes, but o8G modifications in circRNAs have not yet been reported. ROS, products of aerobic metabolism

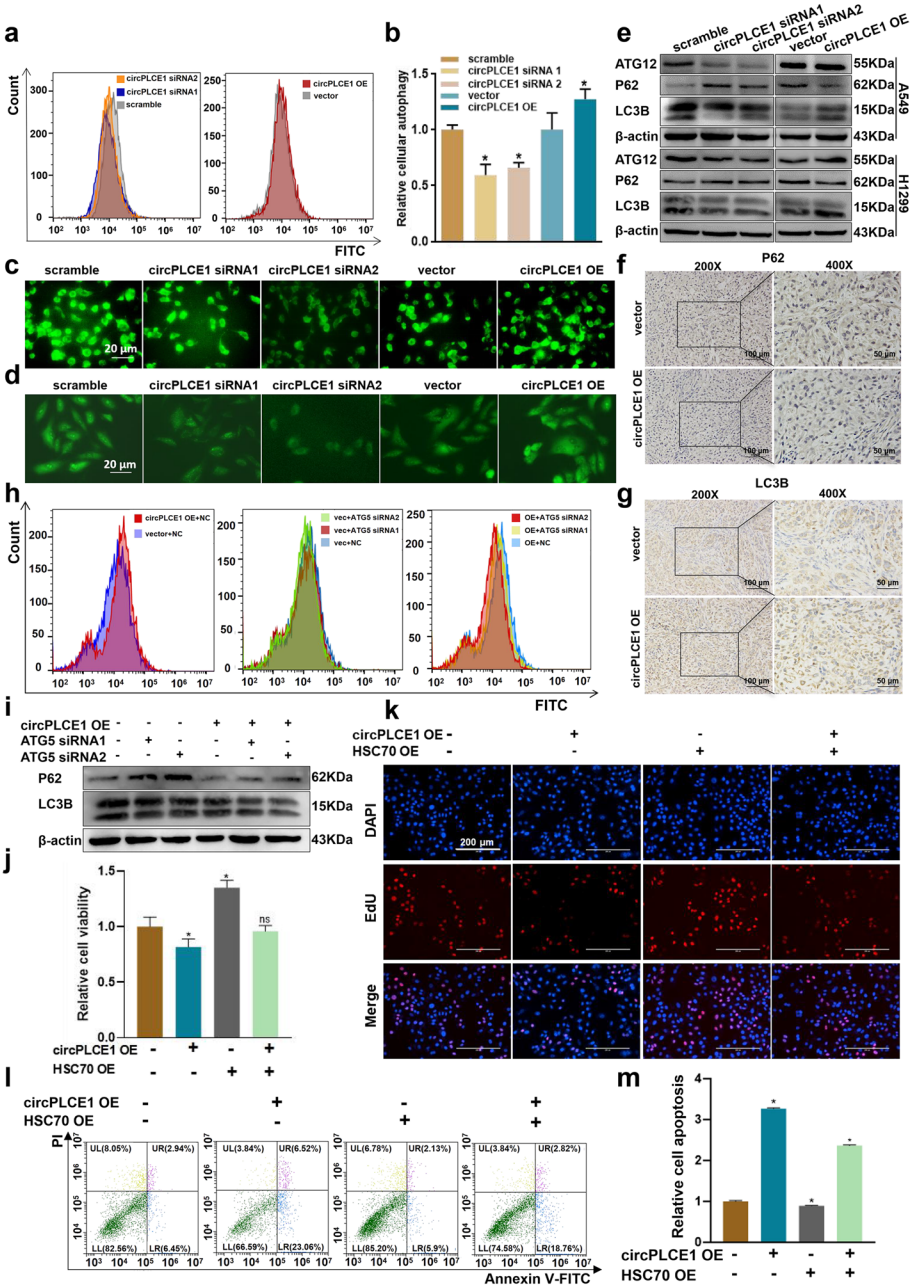

Fig. 7 circPLCE1 inhibits lung cancer progression by targeting HSC70 and regulates ATG5-dependent macroautophagy via the CMA pathway. **a** After circPLCE1 silencing/overexpression in A549 cells, cellular autophagy was detected via flow cytometry. **b** Statistical analysis of the cellular autophagy levels. **c** After cirPLCE1 silencing/overexpression in A549 cells, cellular autophagy was detected via MDC staining. **d** After cirPLCE1 silencing/overexpression in A549 cells, cellular autophagy was detected via CYTO-ID staining. **e** After circPLCE1 silencing/overexpression in A549 cells, ATG12, P62 and LC3B protein expression levels were detected via WB analysis. **f** Immunohistochemistry was performed to evaluate P62 protein expression in nude mouse tumours. **g** Immunohistochemistry was performed to evaluate LC3B expression in nude mouse tumours. **h** Flow cytometry was performed to determine the proportion of cell undergoing autophagy after circPLCE1 was overexpressed and ATG5 was silenced in A549 cells. **i** WB was performed to detect P62 and LC3B protein expression levels after circPLCE1 was overexpressed and ATG5 was silenced in A549 cells. **j** After circPLCE1 and HSC70 were overexpressed in A549 cells, a CCK-8 assay was performed to evaluate cell viability. **k** After circPLCE1 and HSC70 were overexpressed in A549 cells, an EdU incorporation assay was performed to determine the cell proliferation capacity. **l** After circPLCE1 and HSC70 were overexpressed in A549 cells, flow cytometry was performed to determine the proportion of apoptotic cells. **m** Statistical analysis of the results of the apoptosis assay after combined overexpression of circPLCE1 and HSC70

(mitochondrial respiration), are involved in all cellular biological activities. The dysregulation of ROS homeostasis caused by environmental stress or pathophysiological conditions can lead to abnormal o8G levels and affect the occurrence and progression of various diseases, including tumours [24–27]. Since exogenous supplementation with H_2O_2 and NAC is currently widely used as a convenient method to modulate intracellular ROS levels [65, 66], in this study, we added exogenous H_2O_2 and NAC to mimic intracellular ROS dysregulation and assessed the o8G modification level after ROS dysregulation. Our results indicate that the circPLCE1 o8G level is closely related to the intracellular ROS level. Although we revealed that ROS can induce o8G modification of circPLCE1, whether the increased o8G modification of circPLCE1 occurs via direct attack of ROS on guanine bases in circPLCE1 or through the insertion of free nucleotides after oxidation remains to be further explored. In addition, further clarification of the specific circPLCE1 o8G modification base sites is needed for subsequent studies.

Studies have shown that o8G modification plays an important role in the regulation of RNA fate. The o8G modification can change the base pairing pattern of an RNA, shifting the original G–C pairing to the G–A pairing, and it has been suggested that o8G modification may also be involved in the regulation of RNA stability. To explore whether o8G modification regulates the molecular fate of circPLCE1, we carried out an in-depth exploration. We found that AUF1 can act as an o8G reader and bind specifically to the o8G modification of circPLCE1, reversing the o8G modification-mediated decrease in circPLCE1 stability after AUF1 silencing. The change in RNA stability mediated by RNA modification is a critical step in the strict regulation of gene expression and is closely associated with various pathological and physiological processes [47]. RNA o8G modifications can lead to altered gene expression through multiple mechanisms, including "nonsense-mediated mRNA decay", "continuous mRNA decay", and "no-go decay (NGD)" [47, 67]. There are also studies indicating that o8G-modified RNAs can be recognized by specific proteins to achieve the selective degradation of RNAs. The RBPs reported in the present study that preferentially recognize o8G modifications are AUF1, YB-1, PNPase, and PCBP1&2 [68–72]. Y-box binding protein 1 (YBX1) has been shown to bind preferentially to o8G modifications, thereby triggering rapid degradation of o8G-modified mRNAs [71]; the AUF1 protein binds specifically to RNA o8G modifications and acts as an o8G reader, mediating RNA decay, and AUF1 preferentially binds oxidized RNA approximately three times more than unmodified RNA [30, 73]. In our study, o8G modifications induced by ROS accumulation led to a decrease in the stability of the tumour suppressor circRNA circPLCE1, thereby promoting lung cancer progression. This result is also consistent with the results of studies on redox imbalance and abnormal increases in o8G modifications in various tumours [74, 75]. Our work provides new insights into the expression and regulatory patterns of circRNAs, but the underlying mechanism by which AUF1 recognizes o8G modifications and decreases the stability of circRNAs needs to be further clarified. Whether o8G modifications can affect the nucleocytoplasmic output of circRNAs and cap-independent translation also needs further exploration. Recently, the role of RNA modifications in major human diseases has been highlighted, with major breakthroughs in biomedical research. Owing to their unique molecular characteristics, circRNAs are also expected to overcome the limitations in the clinical transformation of linear RNAs related to instability [76]. Therefore, in-depth exploration of circRNAs and their chemical modifications will be beneficial for developing highly specific and long-term approaches for tumour treatment.

Numerous studies have revealed that the direct binding of circRNAs to proteins is an important mechanism by which circRNAs function in tumours [48–50]. Our results revealed that circPLCE1 binds directly to HSC70 and reduces its stability. HSC70 is a molecular chaperone heat shock protein (HSP) whose primary function is protein quality control through its activity as a folding catalyst or in targeting misfolded proteins for degradation, and it is also a key protein in CMA [51]. Two key proteins of CMA, LAMP2A and HSC70, are significantly overexpressed in lung cancer, and both are independent markers of a poor prognosis for lung cancer, which is consistent with the trend of circPLCE1 as a cancer suppressor [77]. Since we focused on changes in HSC70 expression in this study, we propose that circPLCE1 targets HSC70, increases HSC70 ubiquitination and reduces HSC70 stability. The ubiquitin–proteasome pathway is an important pathway of endogenous protein degradation in which proteins to be degraded are modified by ubiquitination and then degraded via the proteasome [78]. Previous studies have revealed that circRNAs can regulate the ubiquitination levels of binding proteins, thereby regulating protein expression. circRNAs can serve as molecular scaffolds for the direct binding of proteins with ubiquitin ligases/deubiquitinates, enhancing the interactions between these proteins and thereby regulating protein ubiquitination levels. circHIPK3 acts as a scaffold to recruit ubiquitin ligases, leading to HuR degradation [16]. circGALNT16 acts as a protein scaffold to enhance the interaction between hnRNPK and SUMO1, thereby inhibiting the progression of colorectal cancer [79]. The TRAP-MS data revealed substantial enrichment of ubiquitin ligases, suggesting that circPLCE1 may act

as a molecular scaffold to enhance interactions between HSC70 and ubiquitin ligases, thus increasing the level of HSC70 ubiquitination. We will continue to explore specific HSC70 ubiquitin ligases and ubiquitination sites in subsequent studies.

Through in-depth exploration of the molecular mechanisms of circPLCE1 in lung cancer, we found that circPLCE1 inhibits CMA activity through HSC70. Previous studies emphasized the role of CMA in protein quality control and suggested that abnormally synthesized or damaged proteins containing a KFERQ motif are the main CMA substrates [80]. However, evidence indicates that most proteins that are functionally intact and contain a KFERQ motif can be degraded via the CMA pathway [39, 81]. The majority of these findings indicate that CMA facilitates tumour cell survival and promotes cancer progression. The activity of CMA is consistently increased in various tumours, such as lung tumours, and CMA can be significantly activated under exposure to external stimuli or conditions, such as nutrient deficiency, hypoxia and oxidative stress [54–56]. After cells were subjected to serum starvation, the protein levels of the classical CMA substrates HK2 and PKM2 were significantly decreased via lysosomal degradation; HK2 and PKM2 are also key rate-limiting enzymes in glycolysis that have been reported to play a role in promoting cancer progression [52]. A large body of evidence indicates that CMA activity facilitates tumour progression, but we found that the expression of HK2 and PKM2, which are also protumorigenic molecules, was negatively correlated with CMA activity. A reasonable explanation for this discrepancy is that the accelerated degradation of proteins such as PKM2 by CMA leads to the accumulation of glycolytic intermediates, which supports the requirements for the rapid proliferation of tumour cells. Related studies on cellular energetics indicate that CMA reduces the overall metabolic activity of cells by selectively degrading functionally intact key enzymes involved in lipid and glucose metabolism, which facilitates the unlimited proliferation of tumour cells to support their survival in a nutrient-limited microenvironment [82].

Our results suggest that ATG5 can act as a CMA substrate and can be degraded via the lysosomal pathway. ATG5 is a key protein involved in phagocytic membrane extension in autophagic vesicles, and it forms a constitutive complex with ATG12. It has been reported that CMA activation downregulates ATG5-dependent macroautophagy, which promotes breast cancer cell metastasis, suggesting a close correlation between ATG5 and CMA activity [83]. This study revealed increased levels of ATG5 mRNA and protein expression after LAMP2A was knocked down in MDA-MB-231 cells, but whether ATG5 can act as a CMA substrate and thus be degraded via the lysosomal pathway has not been elucidated. In the current study in lung cancer cells, we did not find a link between CMA activity and the ATG5 mRNA expression level (Supplementary Fig. 4e), which may be related to the differences in autophagy patterns in cells from different tumours. Our study demonstrated that circPLCE1-mediated inhibition of CMA activity leads to increased ATG5 expression levels and increased macroautophagy, thereby inhibiting lung cancer progression. Many research groups have reported the inhibitory role of ATG5-related macroautophagy in lung cancer and other cancers. For example, macroautophagy promotion due to DDX24 loss inhibits lung cancer growth [58]. Muyin extract (MSE) treatment significantly promotes macroautophagy and increases ATG-5 and Beclin-1 levels and the LC3II/I ratio; it also inhibits NSCLC cell proliferation [59]. The ACSS2/SIRT1/ATG5/ATG2B axis activates macroautophagy and inhibits OC progression in vitro and in vivo [60]. Therefore, to explore the role of HSC70-mediated CMA downregulation in lung cancer, we designed rescue experiments that targeted CMA activity. Increasing evidence indicates a close association between CMA and macroautophagy [57]. Compensatory macroautophagy can help CMA-deficient cells maintain normal protein degradation processes and viability. In the PC12 cell model, pathogenic α-congruent nucleoprotein mutant-mediated inhibition of CMA led to compensatory activation of macroautophagy, which compensated for the protein degradation function of CMA [84]; CMA dysfunction due to the presence of A53T mutant α-synuclein in cortical neurons and differentiated SHSY5Y cells can also lead to increased macroautophagic activity [85]. However, the mechanism underlying the interaction between CMA and macroautophagy has not been elucidated. There are complex mechanisms of interaction between CMA and macroautophagy; however, the study of crosstalk between macroautophagy and CMA is still in an early stage. Elucidating the compensatory mechanism between these two autophagic pathways will provide additional support for exploring effective tumour interventions that target autophagy.

In summary, the present study reveals the existence of o8G modifications on circRNAs and the important role of o8G-modified circRNAs in lung cancer progression. We identified AUF1 as a reader that recognizes the ROS-induced o8G modification of circPLCE1 and reduces its stability. We elucidated a novel molecular mechanism by which circPLCE1 targets the HSC70 protein, increases its ubiquitination level, inhibits CMA activity, and promotes ATG5-dependent macroautophagy via the CMA pathway, altering the fate of tumour cells and ultimately inhibiting lung cancer progression. Our study provides new insights into the molecular mechanisms of lung cancer progression as well as potential targets for lung cancer therapy.

Supplementary Information

The online version contains supplementary material available at https://doi.org/10.1186/s12943-025-02283-0.

Supplementary Material 1

Supplementary Material 2

Supplementary Material 3

Supplementary Material 4

Supplementary Material 5: Fig. S1 circPLCE1 significantly inhibits lung cancer progression *in vivo* and *in vitro*. a. circPLCE1-targeted binding proteins were identified and analysed via KEGG to predict the biological function of circPLCE1. b. circPLCE1-targeted mRNAs were identified and analysed via KEGG to predict the biological function of circPLCE1. c. circPLCE1 transient overexpression plasmid profile. d. circPLCE1 stable overexpression plasmid profile. e. qPCR analysis of the circPLCE1 transient silencing/overexpression efficiency. f. Measurement of PLCE1 mRNA expression via qPCR after transient silencing/overexpression of circPLCE1. g. Wound healing assay to evaluate cell migration ability after circPLCE1 silencing/overexpression. h. Statistical analysis of the wound healing assay results. Fig. S2 circPLCE1 targets the HSC70 protein. a. Schematic diagram of the TRAP experiment. b. Predicting proteins with direct RNA-binding ability in the MS data. c. TRAP-MS was carried out to identify the direct binding proteins of circPLCE1, and an MA plot (M-versus-A plot) of TRAP-MS was generated. d. Quantitative analysis of the immunohistochemistry results. e. HSC70 gene expression levels in lung adenocarcinoma. f. HSC70 gene expression levels in lung squamous cell carcinoma. g. Measurement of the HSC70 mRNA expression level via qPCR after circPLCE1 silencing/overexpression. h. qPCR analysis of AUF1 silencing efficiency. i. Statistical analysis of HSC70 WB data after 200 μM H_2O_2 treatment combined with AUF1 silencing in A549 cells. Fig. S3 circPLCE1 regulates the CMA pathway by targeting HSC70. A Statistical analysis of HK2 WB data after serum starvation. b. Statistical analysis of the PKM2 WB data after serum starvation. c. Statistical analysis of the HK2 WB data after AR7 treatment. d. Statistical analysis of the PKM2 WB data after treatment. e. A549 cells were treated with 10 μM and 20 μM AR7, collected at 0, 16, and 24 h and lysed to obtain total protein; the HK2 protein levels were detected via WB. f. A549 cells were treated with 10 μM and 20 μM AR7, collected at 0, 16, and 24 h and lysed to obtain total protein; the PKM2 protein levels were detected via WB. g. Statistical analysis of HK2 WB data after circPLCE1 silencing/overexpression. h. Statistical analysis of the PKM2 WB data after circPLCE1 silencing/overexpression. i. Statistical analysis of the results of the immunohistochemical staining for HK2 and PKM2. j. The efficiency of HSC70 overexpression was assessed via qPCR. k. Statistical analysis of HK2 WB data after circPLCE1 overexpression and AR7 treatment. l. Statistical analysis of the PKM2 WB data after circPLCE1 overexpression and AR7 treatment. m. Statistical analysis of HK2 WB data after combined overexpression of circPLCE1 and HSC70. n. Statistical analysis of the PKM2 WB data after combined overexpression of circPLCE1 and HSC70. o. Statistical analysis of the number of fluorescent spots. Fig. S4 circPLCE1 regulates ATG5 protein expression through the CMA pathway. a. Prediction of the interactions of HSC70 with key proteins involved in macroautophagy. b. Statistical analysis of the ATG5 WB data after serum starvation. c. Statistical analysis of the ATG5 WB data after treatment with AR7. d. A549 cells were treated with 10 μM and 20 μM AR7, cells were lysed to obtain total protein at 0, 16, and 24 h, and ATG5 protein levels were detected via WB. e. A549 cells were treated with 10 μM and 20 μM AR7 and collected at 0, 16 and 24 hours to extract RNA, and a qPCR assay was carried out to detect ATG5 mRNA levels. f. Statistical analysis of the results of the immunohistochemical staining for ATG5. g. Statistical analysis of the ATG5 WB data after circPLCE1 overexpression and AR7 treatment. h. Statistical analysis of the ATG5 WB data after combined overexpression of circPLCE1 and HSC70. Fig. S5 circPLCE1 targets HSC70 and regulates ATG5-dependent macroautophagy, thereby inhibiting lung cancer progression. A Statistical analysis of the ATG12 WB data after circPLCE1 silencing/overexpression. b. Statistical analysis of P62 WB data after circPLCE1 silencing/overexpression. c. Statistical analysis of the LC3B WB data after circPLCE1 silencing/overexpression. d. Statistical analysis of the immunohistochemical staining for P62 and LC3B. e. WB was performed to detect P62 and LC3B expression levels in nude mouse tumours. f. qPCR analysis of the ATG5 silencing efficiency. g. Silencing of ATG5 in A549 cells and detection of ATG5 protein expression levels via WB. h. Statistical analysis of the autophagy assay results after the overexpression of circPLCE1 with the silencing of ATG5. i. Statistical analysis of the P62 and LC3B WB data after the overexpression of circPLCE1 with the silencing of ATG5. j. Detection of cellular autophagy by flow cytometry after combined overexpression of HSC70 and circPLCE1. k. Statistical analysis of the results of the cellular autophagy assay after combined overexpression of circPLCE1 and HSC70. l. Statistical analysis of the EdU incorporation assay results after combined overexpression of circPLCE1 and HSC70.

Supplementary Material 6

Acknowledgements
We thank doctor Huafu Zhou and Jun Liu from the first Affiliated Hospital of Guangxi Medical University, Nanning, Guangxi, China for their support and assistance in the collection of clinical samples.

Authors' contributions
ARN conceived and designed this study. GL supervised and guided the study. QYZ, DYC and HTXperformed the experiments and wrote the manuscript. YHG, RRZ, SXC, JXW, XCC and WYP collected the clinical samples and analysed the data. DYC, XDZ, XCC, SYY and DQL supplemented the experiment and revised the manuscript. ARN and GL guided the revision of this article. All the authors reviewed and approved the final manuscript.

Funding
This work was partially supported by the National Natural Science Foundation of China (NSFC82260652), Natural Science Foundation of Guangxi (2023GXNSFFA026006) and Guangxi Science and Technology Base and Talent Special Project (AD22080055).

Data availability
The circRNA sequencing results have been uploaded to the GEO database (PRJNA971588). At the same time, all data is provided within supplementary information files.

Declarations

Ethics approval and consent to participate
The lung cancer and paraneoplastic clinical tissue samples used in this study were obtained from the First Affiliated Hospital of Guangxi Medical University. All patients signed an informed consent form before surgery. Human materials were obtained with patient consent and approved by the Ethics Committee of the First Affiliated Hospital of Guangxi Medical University (No.2022-KY-E-(289)). All animal experiments were approved by the Animal Ethics Committee of Guangxi Medical University (No. 202401002).

Consent for publication
All of the authors have written informed consent.

Competing interests
The authors declare no competing interests.

Author details
[1]School of Public Health, Guangxi Medical University, Nanning 530021, China. [2]Guangxi Key Laboratory of Environment and Health Research, Guangxi Medical University, Nanning 530021, China.

Received: 29 August 2024 Accepted: 25 February 2025
Published online: 17 March 2025

References

1. Siegel RL, Wagle NS, Cercek A, Smith RA, Jemal A. Colorectal cancer statistics, 2023. CA Cancer J Clin. 2023;73:233–54.

2. Bray F, Laversanne M, Sung H, Ferlay J, Siegel RL, Soerjomataram I, et al. Global cancer statistics 2022: GLOBOCAN estimates of incidence and mortality worldwide for 36 cancers in 185 countries. CA Cancer J Clin. 2024;74:229–63.
3. Lahiri A, Maji A, Potdar PD, Singh N, Parikh P, Bisht B, et al. Lung cancer immunotherapy: progress, pitfalls, and promises. Mol Cancer. 2023;22:40.
4. Ruiz-Cordero R, Devine WP. Targeted Therapy and Checkpoint Immunotherapy in Lung Cancer. Surg Pathol Clin. 2020;13:17–33.
5. Tan AC, Tan DSW. Targeted Therapies for Lung Cancer Patients With Oncogenic Driver Molecular Alterations. J Clin Oncol. 2022;40:611–25.
6. Rasmi RR, Sakthivel KM, Guruvayoorappan C. NF-kappaB inhibitors in treatment and prevention of lung cancer. Biomed Pharmacother. 2020;130:110569.
7. Zarredar H, Ansarin K, Baradaran B, Shekari N, Eyvazi S, Safari F, et al. Critical microRNAs in Lung Cancer: Recent Advances and Potential Applications. Anticancer Agents Med Chem. 2018;18:1991–2005.
8. Wang C, Tan S, Li J, Liu WR, Peng Y, Li W. CircRNAs in lung cancer - Biogenesis, function and clinical implication. Cancer Lett. 2020;492:106–15.
9. Liu CX, Chen LL. Circular RNAs: Characterization, cellular roles, and applications. Cell. 2022;185:2016–34.
10. Patop IL, Wust S, Kadener S. Past, present, and future of circRNAs. EMBO J. 2019;38:e100836.
11. Kristensen LS, Jakobsen T, Hager H, Kjems J. The emerging roles of circRNAs in cancer and oncology. Nat Rev Clin Oncol. 2022;19:188–206.
12. Zhang Q, Wang W, Zhou Q, Chen C, Yuan W, Liu J, et al. Roles of circRNAs in the tumour microenvironment. Mol Cancer. 2020;19:14.
13. Zhen N, Gu S, Ma J, Zhu J, Yin M, Xu M, et al. CircHMGCS1 Promotes Hepatoblastoma Cell Proliferation by Regulating the IGF Signaling Pathway and Glutaminolysis. Theranostics. 2019;9:900–19.
14. Liang Y, Wang H, Chen B, Mao Q, Xia W, Zhang T, et al. circDCUN1D4 suppresses tumor metastasis and glycolysis in lung adenocarcinoma by stabilizing TXNIP expression. Mol Ther Nucleic Acids. 2021;23:355–68.
15. Shi L, Liu B, Shen DD, Yan P, Zhang Y, Tian Y, et al. A tumor-suppressive circular RNA mediates uncanonical integrin degradation by the proteasome in liver cancer. Sci Adv. 2021;7:eabe5043.
16. Ding F, Lu L, Wu C, Pan X, Liu B, Zhang Y, et al. circHIPK3 prevents cardiac senescence by acting as a scaffold to recruit ubiquitin ligase to degrade HuR. Theranostics. 2022;12:7550–66.
17. Shi Y, Jia X, Xu J. The new function of circRNA: translation. Clin Transl Oncol. 2020;22:2162–9.
18. Li X, Chen S, Wang X, Zhang R, Yang J, Xu H, et al. The pivotal regulatory factor circBRWD1 inhibits arsenic exposure-induced lung cancer occurrence by binding mRNA and regulating its stability. Mol Ther Oncolytics. 2022;26:399–412.
19. Teng PC, Liang Y, Yarmishyn AA, Hsiao YJ, Lin TY, Lin TW, et al. RNA Modifications and Epigenetics in Modulation of Lung Cancer and Pulmonary Diseases. Int J Mol Sci. 2021;22:10592.
20. Shi H, Wei J, He C. Where, When, and How: Context-Dependent Functions of RNA Methylation Writers, Readers, and Erasers. Mol Cell. 2019;74:640–50.
21. Roundtree IA, Evans ME, Pan T, He C. Dynamic RNA Modifications in Gene Expression Regulation. Cell. 2017;169:1187–200.
22. Barbieri I, Kouzarides T. Role of RNA modifications in cancer. Nat Rev Cancer. 2020;20:303–22.
23. Li C, Xue Y, Ba X, Wang R. The Role of 8-oxoG Repair Systems in Tumorigenesis and Cancer Therapy. Cells. 2022;11:3798.
24. Wang JX, Gao J, Ding SL, Wang K, Jiao JQ, Wang Y, et al. Oxidative Modification of miR-184 Enables It to Target Bcl-xL and Bcl-w. Mol Cell. 2015;59:50–61.
25. Seok H, Lee H, Lee S, Ahn SH, Lee HS, Kim GD, et al. Position-specific oxidation of miR-1 encodes cardiac hypertrophy. Nature. 2020;584:279–85.
26. Eom S, Peak J, Park J, Ahn SH, Cho YK, Jeong Y, et al. Widespread 8-oxoguanine modifications of miRNA seeds differentially regulate redox-dependent cancer development. Nat Cell Biol. 2023;25:1369–83.
27. Graille M, Seraphin B. Surveillance pathways rescuing eukaryotic ribosomes lost in translation. Nat Rev Mol Cell Biol. 2012;13:727–35.
28. Jamar NH, Kritsiligkou P, Grant CM. The non-stop decay mRNA surveillance pathway is required for oxidative stress tolerance. Nucleic Acids Res. 2017;45:6881–93.
29. Simms CL, Hudson BH, Mosior JW, Rangwala AS, Zaher HS. An active role for the ribosome in determining the fate of oxidized mRNA. Cell Rep. 2014;9:1256–64.
30. Ishii T, Hayakawa H, Sekiguchi T, Adachi N, Sekiguchi M. Role of Auf1 in elimination of oxidatively damaged messenger RNA in human cells. Free Radic Biol Med. 2015;79:109–16.
31. Wang Y, Mo Y, Peng M, Zhang S, Gong Z, Yan Q, et al. The influence of circular RNAs on autophagy and disease progression. Autophagy. 2022;18:240–53.
32. Levine B, Kroemer G. Biological Functions of Autophagy Genes: A Disease Perspective. Cell. 2019;176:11–42.
33. Glick D, Barth S, Macleod KF. Autophagy: cellular and molecular mechanisms. J Pathol. 2010;221:3–12.
34. Filomeni G, De Zio D, Cecconi F. Oxidative stress and autophagy: the clash between damage and metabolic needs. Cell Death Differ. 2015;22:377–88.
35. D'Arcy MS. Cell death: a review of the major forms of apoptosis, necrosis and autophagy. Cell Biol Int. 2019;43:582–92.
36. Yamamoto H, Matsui T. Molecular Mechanisms of Macroautophagy, Microautophagy, and Chaperone-Mediated Autophagy. J Nippon Med Sch. 2024;91:2–9.
37. Chen X, Mao R, Su W, Yang X, Geng Q, Guo C, et al. Circular RNA circHIPK3 modulates autophagy via MIR124-3p-STAT3-PRKAA/AMPKalpha signaling in STK11 mutant lung cancer. Autophagy. 2020;16:659–71.
38. Zhu T, Cen Y, Chen Z, Zhang Y, Zhao L, Wang J, et al. Oncogenic circTICRR suppresses autophagy via binding to HuR protein and stabilizing GLUD1 mRNA in cervical cancer. Cell Death Dis. 2022;13:479.
39. Kaushik S, Cuervo AM. The coming of age of chaperone-mediated autophagy. Nat Rev Mol Cell Biol. 2018;19:365–81.
40. Kon M, Kiffin R, Koga H, Chapochnick J, Macian F, Varticovski L, et al. Chaperone-mediated autophagy is required for tumor growth. Sci Transl Med 2011;3:109ra117.
41. Du W, Xu A, Huang Y, Cao J, Zhu H, Yang B, et al. The role of autophagy in targeted therapy for acute myeloid leukemia. Autophagy. 2021;17:2665–79.
42. Vilema-Enriquez G, Arroyo A, Grijalva M, Amador-Zafra RI, Camacho J. Molecular and Cellular Effects of Hydrogen Peroxide on Human Lung Cancer Cells: Potential Therapeutic Implications. Oxid Med Cell Longev. 2016;2016:1908164.
43. Park WH. MAPK inhibitors, particularly the JNK inhibitor, increase cell death effects in H2O2-treated lung cancer cells via increased superoxide anion and glutathione depletion. Oncol Rep. 2018;39:860–70.
44. Wiel C, Le Gal K, Ibrahim MX, Jahangir CA, Kashif M, Yao H, et al. BACH1 Stabilization by Antioxidants Stimulates Lung Cancer Metastasis. Cell. 2019;178:330-345 e322.
45. Kim KC, Ruwan Kumara MHS, Kang KA, Piao MJ, Oh MC, Ryu YS, et al. Exposure of keratinocytes to non-thermal dielectric barrier discharge plasma increases the level of 8-oxoguanine via inhibition of its repair enzyme. Mol Med Rep. 2017;16:6870–5.
46. Boo SH, Kim YK. The emerging role of RNA modifications in the regulation of mRNA stability. Exp Mol Med. 2020;52:400–8.
47. Ishii T, Sekiguchi M. Two ways of escaping from oxidative RNA damage: Selective degradation and cell death. DNA Repair (Amst). 2019;81:102666.
48. Li B, Zhu L, Lu C, Wang C, Wang H, Jin H, et al. circNDUFB2 inhibits non-small cell lung cancer progression via destabilizing IGF2BPs and activating anti-tumor immunity. Nat Commun. 2021;12:295.
49. Holdt LM, Stahringer A, Sass K, Pichler G, Kulak NA, Wilfert W, et al. Circular non-coding RNA ANRIL modulates ribosomal RNA maturation and atherosclerosis in humans. Nat Commun. 2016;7:12429.
50. Du WW, Yang W, Liu E, Yang Z, Dhaliwal P, Yang BB. Foxo3 circular RNA retards cell cycle progression via forming ternary complexes with p21 and CDK2. Nucleic Acids Res. 2016;44:2846–58.
51. Stricher F, Macri C, Ruff M, Muller S. HSPA8/HSC70 chaperone protein: structure, function, and chemical targeting. Autophagy. 2013;9:1937–54.
52. Lv L, Li D, Zhao D, Lin R, Chu Y, Zhang H, et al. Acetylation targets the M2 isoform of pyruvate kinase for degradation through chaperone-mediated autophagy and promotes tumor growth. Mol Cell. 2011;42:719–30.
53. Xia HG, Najafov A, Geng J, Galan-Acosta L, Han X, Guo Y, et al. Degradation of HK2 by chaperone-mediated autophagy promotes metabolic catastrophe and cell death. J Cell Biol. 2015;210:705–16.
54. Cuervo AM, Knecht E, Terlecky SR, Dice JF. Activation of a selective pathway of lysosomal proteolysis in rat liver by prolonged starvation. Am J Physiol. 1995;269:C1200-1208.

55. Kiffin R, Christian C, Knecht E, Cuervo AM. Activation of chaperone-mediated autophagy during oxidative stress. Mol Biol Cell. 2004;15:4829–40.
56. Dohi E, Tanaka S, Seki T, Miyagi T, Hide I, Takahashi T, et al. Hypoxic stress activates chaperone-mediated autophagy and modulates neuronal cell survival. Neurochem Int. 2012;60:431–42.
57. Wu H, Chen S, Ammar AB, Xu J, Wu Q, Pan K, et al. Crosstalk Between Macroautophagy and Chaperone-Mediated Autophagy: Implications for the Treatment of Neurological Diseases. Mol Neurobiol. 2015;52:1284–96.
58. Sun S, Jing X, Tong G, Chen C, Xie S, Wang C, et al. Loss of DDX24 inhibits lung cancer progression by stimulating IKBKG splicing-mediated autophagy. Theranostics. 2025;15:1879–95.
59. Kan Y, Song M, Cui X, Yang Q, Zang Y, Li Q, et al. Muyin extract inhibits non-small-cell lung cancer growth by inducing autophagy and apoptosis in vitro and in vivo. Phytomedicine. 2022;96:153834.
60. Yang J, Wang H, Li B, Liu J, Zhang X, Wang Y, et al. Inhibition of ACSS2 triggers glycolysis inhibition and nuclear translocation to activate SIRT1/ATG5/ATG2B deacetylation axis, promoting autophagy and reducing malignancy and chemoresistance in ovarian cancer. Metabolism. 2025;162:156041.
61. Anastasiadou E, Jacob LS, Slack FJ. Non-coding RNA networks in cancer. Nat Rev Cancer. 2018;18:5–18.
62. Cech TR, Steitz JA. The noncoding RNA revolution-trashing old rules to forge new ones. Cell. 2014;157:77–94.
63. Liang ZX, Liu HS, Xiong L, Yang X, Wang FW, Zeng ZW, et al. A novel NF-kappaB regulator encoded by circPLCE1 inhibits colorectal carcinoma progression by promoting RPS3 ubiquitin-dependent degradation. Mol Cancer. 2021;20:103.
64. Kong Q, Lin CL. Oxidative damage to RNA: mechanisms, consequences, and diseases. Cell Mol Life Sci. 2010;67:1817–29.
65. Rivas-Chacon LDM, Martinez-Rodriguez S, Madrid-Garcia R, Yanes-Diaz J, Riestra-Ayora JI, Sanz-Fernandez R, et al. Role of Oxidative Stress in the Senescence Pattern of Auditory Cells in Age-Related Hearing Loss. Antioxidants (Basel). 2021;10:1497.
66. Liu ZJ, Zhao W, Zhang QG, Li L, Lai LY, Jiang S, et al. OGG1 Involvement in High Glucose-Mediated Enhancement of Bupivacaine-Induced Oxidative DNA Damage in SH-SY5Y Cells. Oxid Med Cell Longev. 2015;2015:683197.
67. Wolin SL, Maquat LE. Cellular RNA surveillance in health and disease. Science. 2019;366:822–7.
68. Taylor KE, Miller LG, Contreras LM. RNA-binding proteins that preferentially interact with 8-oxoG-modified RNAs: our current understanding. Biochem Soc Trans. 2024;52:111–22.
69. Hayakawa H, Kuwano M, Sekiguchi M. Specific binding of 8-oxoguanine-containing RNA to polynucleotide phosphorylase protein. Biochemistry. 2001;40:9977–82.
70. Seixas AF, Quendera AP, Sousa JP, Silva AFQ, Arraiano CM, Andrade JM. Bacterial Response to Oxidative Stress and RNA Oxidation. Front Genet. 2021;12:821535.
71. Hayakawa H, Uchiumi T, Fukuda T, Ashizuka M, Kohno K, Kuwano M, et al. Binding capacity of human YB-1 protein for RNA containing 8-oxoguanine. Biochemistry. 2002;41:12739–44.
72. Ishii T, Igawa T, Hayakawa H, Fujita T, Sekiguchi M, Nakabeppu Y. PCBP1 and PCBP2 both bind heavily oxidized RNA but cause opposing outcomes, suppressing or increasing apoptosis under oxidative conditions. J Biol Chem. 2020;295:12247–61.
73. Malfatti MC, Codrich M, Dalla E, D'Ambrosio C, Storici F, Scaloni A, et al. AUF1 Recognizes 8-Oxo-Guanosine Embedded in DNA and Stimulates APE1 Endoribonuclease Activity. Antioxid Redox Signal. 2023;39:411–31.
74. Filaire E, Dupuis C, Galvaing G, Aubreton S, Laurent H, Richard R, et al. Lung cancer: what are the links with oxidative stress, physical activity and nutrition. Lung Cancer. 2013;82:383–9.
75. Kawanishi S, Ohnishi S, Ma N, Hiraku Y, Oikawa S, Murata M. Nitrative and oxidative DNA damage in infection-related carcinogenesis in relation to cancer stem cells. Genes Environ. 2016;38:26.
76. Dolgin E. Why rings of RNA could be the next blockbuster drug. Nature. 2023;622:22–4.
77. Losmanova T, Janser FA, Humbert M, Tokarchuk I, Schlafli AM, Neppl C, et al. Chaperone-Mediated Autophagy Markers LAMP2A and HSC70 Are Independent Adverse Prognostic Markers in Primary Resected Squamous Cell Carcinomas of the Lung. Oxid Med Cell Longev. 2020;2020:8506572.
78. Pickart CM, Eddins MJ. Ubiquitin: structures, functions, mechanisms. Biochim Biophys Acta. 2004;1695:55–72.
79. Peng C, Tan Y, Yang P, Jin K, Zhang C, Peng W, et al. Circ-GALNT16 restrains colorectal cancer progression by enhancing the SUMOylation of hnRNPK. J Exp Clin Cancer Res. 2021;40:272.
80. Schneider JL, Suh Y, Cuervo AM. Deficient chaperone-mediated autophagy in liver leads to metabolic dysregulation. Cell Metab. 2014;20:417–32.
81. Hubert V, Weiss S, Rees AJ, Kain R. Modulating Chaperone-Mediated Autophagy and Its Clinical Applications in Cancer. Cells. 2022;11:2562.
82. Kaushik S, Cuervo AM. Degradation of lipid droplet-associated proteins by chaperone-mediated autophagy facilitates lipolysis. Nat Cell Biol. 2015;17:759–70.
83. Han Q, Deng Y, Chen S, Chen R, Yang M, Zhang Z, et al. Downregulation of ATG5-dependent macroautophagy by chaperone-mediated autophagy promotes breast cancer cell metastasis. Sci Rep. 2017;7:4759.
84. Cuervo AM, Stefanis L, Fredenburg R, Lansbury PT, Sulzer D. Impaired degradation of mutant alpha-synuclein by chaperone-mediated autophagy. Science. 2004;305:1292–5.
85. Xilouri M, Vogiatzi T, Vekrellis K, Park D, Stefanis L. Abberant alpha-synuclein confers toxicity to neurons in part through inhibition of chaperone-mediated autophagy. PLoS ONE. 2009;4:e5515.

Publisher's Note